

Time-dependent lepto-hadronic modeling of the emission from blazar jets with *SOPRANO*: the case of TXS 0506+056, 3HSP J095507.9+355101 and 3C 279

S. Gasparyan^{1*}, D. Bégué^{2,3 †} & N. Sahakyan^{1,4,5 ‡}

¹ ICRA Net-Armenia, Marshall Baghramian Avenue 24a, Yerevan 0019, Armenia

² Department of Physics, Bar Ilan University, Ramat-Gan 52900, Israel §

³ Max-Planck-Institut für extraterrestrische Physik, Giessenbachstrasse, D-85748 Garching, Germany

⁴ ICRA Net, P.zza della Repubblica 10, 65122 Pescara, Italy

⁵ ICRA, Dipartimento di Fisica, Sapienza Università di Roma, P.le Aldo Moro 5, 00185 Rome, Italy

Accepted XXX. Received YYY; in original form ZZZ

ABSTRACT

The observation of a very-high-energy neutrino by IceCube (IceCube-170922A) and its association with the flaring blazar TXS 0506+056 provided the first multimessenger observations of blazar jets, demonstrating the important role of protons in their dynamics and emission. In this paper, we present *SOPRANO* (<https://www.amsdc.am/soprano>), a new conservative implicit kinetic code which follows the time evolution of the isotropic distribution functions of protons, neutrons and the secondaries produced in photo-pion and photo-pair interactions, alongside with the evolution of photon and electron/positron distribution functions. *SOPRANO* is designed to study leptonic and hadronic processes in relativistic sources such as blazars and gamma-ray bursts. Here, we use *SOPRANO* to model the broadband spectrum of TXS 0506+056 and 3HSP J095507.9+355101, which are associated with neutrino events, and of the extreme flaring blazar 3C 279. The SEDs are interpreted within the guise of both a hadronic and a hybrid model. We discuss the implications of our assumptions in terms of jet power and neutrino flux.

Key words: Radiation mechanisms: non-thermal – quasars: individual: TXS 0506+056, 3HSP J095507.9+355101 and 3C 279 – galaxies: jets – gamma-rays: galaxies

1 INTRODUCTION

The discovery of the first cosmic very high energy (VHE; > 100 GeV) neutrinos in 2013 by the IceCube experiment (IceCube Collaboration 2013; Aartsen et al. 2013; Aartsen et al. 2020) has opened a new window on VHE sources such as gamma-ray bursts (hereafter GRBs), active galactic nuclei (AGNs) and tidal disruption events (TDEs). The lack of high confidence association between these neutrino events and a particular type of sources significantly complicated the interpretation of their origin. Potentially, they are produced in the sources where ultra-high energy cosmic rays (protons or nucleons with energy exceeding 10^{19} eV) are accelerated. If the origin of these neutrinos remains an open question, the VHE neutrino event IceCube 170922A (IceCube Collaboration et al. 2018a) and its 3.5σ association with the (simultaneously) flaring blazar TXS 0506+056 (IceCube Collaboration et al. 2018b; Padovani et al. 2018) made clear that high energy (HE; > 100 MeV) protons, neutrons and even possibly nucleons have an important role to play in the dynamics and the radiation of relativistic jets (Begelman et al. 1990; Sikora et al. 1996; Atoyan & Dermer 2003).

Blazars are a subclass of AGNs which have their jet aligned

with or making a small angle to the observer (Urry & Padovani 1995). Blazars are among the most luminous and energetic sources in the Universe. Based on optical emission lines blazars are sub-grouped as flat spectrum radio quasars (FSRQs) and BL Lacs: the emission lines are strong and quasar-like in FSRQs and weak or absent in BL lacs (Urry & Padovani 1995). The emission from blazar jets, extending from radio to HE and VHE γ -ray bands (Padovani et al. 2017), is characterized by rapid and high amplitude variability, especially in the HE and VHE γ -ray bands (e.g., Aleksić et al. 2014a; Ackermann et al. 2016). This variability suggests that the emission originates from a compact relativistically moving region. Since the γ -ray emission has been detected even from blazars at very high redshift, $z > 3.1$, (e.g., Paliya et al. 2016; Ackermann et al. 2017; Sahakyan et al. 2020), they are unique objects to study the evolution of jet power, morphology and emission processes in different cosmic epochs.

The broadband spectral energy distribution (SED) of blazars typically exhibit a double hump distribution, the first one peaking at optical/UV or X-ray bands (low energy component) and the other one in the HE or VHE γ -ray bands (HE component). The low energy component is usually explained by synchrotron radiation of relativistic electrons in the jet magnetic field. The origin of the HE component is still under debate, mostly between two main scenarios. In leptonic scenarios, the HE component is due to inverse Compton scattering of low energy seed photons by the relativistic

* Corresponding author : sargisganyan@gmail.com

† E-mail: cayley38@gmail.com

‡ E-mail: narek@icra.it

§ Current address.

electrons in the blazar jet (Ghisellini et al. 1985; Maraschi et al. 1992; Bloom & Marscher 1996). The nature of the seed photons depends on the location of the emission region and can be produced either inside or outside the jet (e.g., Sikora et al. 2009). In the alternative hadronic scenarios, synchrotron radiation from protons, see e.g. Mücke & Protheroe (2001), and secondaries generated in photo-pion and photo-pair interactions produce the emission from the X-ray to the HE γ -rays bands (Mannheim 1993; Mannheim & Biermann 1989; Mücke et al. 2003). In addition, inelastic pp scattering could be involved when the highly energetic protons of the jet interact with a dense proton target, such as clouds in the broad line region or surrounding stars (e.g. Dar & Laor (1997); Beall & Bednarek (1999); Araudo et al. (2013)).

Protons are unavoidably accelerated with the electrons in the jet, but a direct test of their presence and energy cannot be done when only considering electromagnetic data. Except for the cases when the leptonic models face severe problems to account for the observed data, usually both leptonic and hadronic models give equally good representation of the data (e.g., Böttcher et al. 2013a). Indirect test of proton content and a proof of the hadronic origin of the HE and VHE emission can only be given by the observation of VHE neutrinos. Indeed, when protons interact within the jet, the energy they lose is nearly equally divided into electromagnetic and neutrinos components. The produced neutrinos escape the emitting region, carrying information about the protons in the jet and their distribution function.

Multimessenger observations have long been considered the next major breakthrough required for the study of extra-galactic objects. The recent association of IceCube 170922A (IceCube Collaboration et al. 2018a) with TXS 0506+056 provided the first ever possibility to perform a direct multimessenger study of a blazar jet. In addition, an analysis of the IceCube archival data revealed a ~ 13 neutrinos excess within a 110 day period, between September 2014 and March 2015, in the direction of TXS 0506+056. Those two pieces of information together suggests that TXS 0506+056 is indeed the source of those HE neutrinos. Moreover, a second possible association between the muon track event IceCube 200107A (IceCube Collaboration 2020) and the blazar 3HSP J095507.9+355101 in a flaring state was reported based on the small angular distance (0.62°) between 3HSP J095507.9+355101 and the best-fit position of IceCube 200107A (Giommi et al. 2020a; Paliya et al. 2020). These two associations provide unprecedented data allowing to constrain the hadronic processes in relativistic jets.

In order to exploit multiwavelength and multimessenger data-sets, several groups have developed numerical models to estimate leptons, hadron and photon distribution functions, either under the steady state approximation (Asano & Inoue 2007; Böttcher et al. 2013b; Cerruti et al. 2015a; Zech et al. 2017), or in a fully time dependent approach (Mastichiadis & Kirk 1995; Pe’er & Waxman 2005; Belmont et al. 2008; Vurm & Poutanen 2009; Dimitrakoudis et al. 2012; Diltz et al. 2015; Gao et al. 2017; Kantzas et al. 2020; Jiménez Fernández & van Eerten 2021) and use them to model the broadband SED of blazars and other relativistic transients. Time-dependent modeling of blazars, both leptonic and hadronic is required to understand the time evolution of particle distribution functions, for instance during a flare, see e.g. Böttcher & Baring (2019).

Time-dependent hadronic modeling is challenging as many different particles are involved. The time evolution of the initial particle populations, as well as that of the secondaries, should be treated with a set of kinetic equations, where the energy is conserved in a self-consistent manner, i.e., the energy lost by a particle is exactly transferred to the energy of other particles. In this paper, we present

and use a new fully time-dependent hadronic code, *SOPRANO*¹, standing for Simulator of Processes in Relativistic AstroNomical Objects, which takes into account all relevant processes (leptonic and hadronic) and allows to compute the SED in any given period. The code solves the time dependent isotropic kinetic equations and preserves the total energy of the system as well as the number of particles where needed. The code structure is modular such that processes can be easily added (or removed). *SOPRANO* is implicit so numerical stability is achieved at all time. The code is designed in a such manner that by changing the initial conditions, the lepto-hadronic processes can be investigated in blazar jets, GRBs and other relativistic astrophysical sources where protons are hypothesized to be efficiently accelerated.

The paper is organised as follow. Section 2 gives a short description of our kinetic code *SOPRANO*. The kinetic processes included in our numerical code and their cross-sections are detailed in Appendix A. The numerical discretization in energy and in time is provided in Appendix B. The analytical estimates of several key model parameters are provided in Section 3 whereas the code is applied to model the broadband SEDs of TXS 0506+056, 3HSP J095507.9+355101 and 3C 279 in Section 4. The discussion is in Section 5, whereas the conclusion is summarized in Section 6. Throughout the paper, we use the definition $X = X_x \times 10^x$ where a quantity X is given in cgs units. Moreover, the following cosmological constants are adopted: $\Omega_M = 0.3$, $\Omega_\Lambda = 0.7$, and $H_0 = 70 \text{ km s}^{-1} \text{ Mpc}^{-1}$ (Freedman et al. 2001).

2 *SOPRANO*: SIMULATOR OF PROCESSES IN RELATIVISTIC ASTRONOMICAL OBJECTS

Investigation of hadronic processes in galactic sources, such as supernovae remnants and pulsar wind nebulae, as well as extra-galactic objects, such as AGNs and GRBs, has always been an interesting but challenging task. Primarily, it is related with the desire to identify the sources in which cosmic rays and ultra-high energy cosmic rays are accelerated, and to understand the processes responsible for the broadband emission. Such studies are especially timely after the recent IceCube observations of cosmic neutrinos and their association with blazars. Indeed, for the first time, it is possible to constrain the emission process using a different window than that of electromagnetic observations.

In order to interpret the observed data and constrain the models that can explain the observed VHE neutrinos, it is necessary to perform self-consistent simulations of the time evolution of the distribution functions of all interacting particles: protons, neutrons, photons, electrons and positrons, as well as of the secondaries produced in photohadronic interactions, such as pions, muons and neutrinos. This is a challenging task since *i*) there is a large number of distribution functions (fourteen even though some are trivial), *ii*) all equations describing the time evolution of particle distribution functions are coupled in a non-trivial and non-linear way by many complex processes that *iii*) have very different time scales, requiring an implicit time discretization. The high number of distribution functions is necessary to compute the cooling and emission of charged secondaries, pions and muons. This requirement also prevents the use of semi-analytical expressions for the production rate of neutrinos, as given in e.g. Kelner & Aharonian (2008)

For blazars, the magnetic field is expected to be around or smaller

¹ <https://www.amsdc.am/soprano>

than 1G for leptonic models (see *e.g.* Finke et al. 2008; Ghisellini & Tavecchio 2009; Tavecchio & Ghisellini 2016; Gasparyan et al. 2018), while hadronic models usually require the magnetic field to be larger, in the range of few tens to few hundreds Gauss (Reynoso et al. 2011; Zech et al. 2017), see however Kusunose & Takahara (2017). This magnetic field is too low to observe a substantial modification of the neutrino spectrum (Bustamante & Tamborra 2020). However, synchrotron cooling of secondaries produces photons, which form pairs, which in turn will radiate, effectively shifting the spectrum to lower-energies for which strong constraints are given by X-ray observatories. In fact, X-ray observations are believed to be the most constraining ones for hadronic models of blazars. In particular, they strongly challenge any models attempting to explain the neutrino emission of TSX 0506+056 (Keivani et al. 2018a; Cerruti et al. 2019b; Gao et al. 2019a; Xue et al. 2019b).

With the goal to model the multiwavelength and multimessenger SED of relativistic sources (e.g., AGNs and GRBs), we have developed a numerical code which computes the temporal evolution of particle distribution functions by solving the relevant kinetic equations. This code, *SOPRANO*, relies on two underlying assumptions: *i*) the space is homogeneous and *ii*) particle distribution functions are isotropic. In its current version, *SOPRANO* uses implicit time discretization to evolve the distribution functions of the following particles:

- (i) photons,
- (ii) electrons and positrons, considered as a single particle type,
- (iii) protons,
- (iv) neutrons,
- (v) charged (π^+ , π^-) and neutral pions (π^0) separately
- (vi) muons
- (vii) neutrinos and anti-neutrinos, all species separately.

The processes considered for the above listed particles are:

- (i) synchrotron emission and cooling of all charged particles (protons, electrons and positrons, charged pions and muons),
- (ii) inverse Compton scattering of photons by electrons and positrons,
- (iii) Bethe-Heitler photo-pair production and corresponding proton cooling,
- (iv) photo-pion production and corresponding cooling of protons and neutrons,
- (v) pion and muon decay,
- (vi) neutrino production.

Detailed expression for the interactions kernel and all terms appearing in the kinetic equations for all particle species are given in Appendix A.

The energy discretization of the fourteen coupled partial differential equations is presented in Appendix B. It follows from the prescription of finite volume allowing us to conserve particle number to machine accuracy for all processes which conserve particle number. For instance, for pion decay, there are as many muons and neutrinos created as pions that decay. Our numerical implementation ensures that $\partial n_\pi / \partial t = -\partial n_\mu / \partial t = -\partial n_\nu / \partial t$. Energy conservation is also enforced by specific choices for the fluxes for diffusion-like terms or redistribution of particles between adjacent energy cells. The difficulty in our numerical implementation is in the computation of the 3- to 5-dimensional integrals which approximate the rates on each energy bin. Each of those integrals are computed to a relative accuracy of 10^{-4} with locally adaptive Gauss-Kronrod method. They only need to be computed one time for a given grid and since we do

not change the energy grid, they remain the same for all the results presented here.

The largely varying time-scale of the processes and the large energy span of particle and photon grids require using an implicit scheme for the time integration. The code uses a semi-implicit version of the backward Euler method, that is to say that for the evaluation of photo-pion and photo-pair collisional terms, the photon spectrum is assumed to be explicit, while the proton and neutron distribution functions are solved for implicitly. This assumption makes the kinetic equation for all hadrons linear by decoupling their evolution from that of the photons and pairs. In practice, it means that the rate of photo-pair and photo-pion interactions might be underestimated, unless the time step is carefully chosen. We have studied how the time step of the integration method should be chosen to minimise the impact on the solution. Then, the kinetic equations describing the evolution of leptons are solved fully implicitly. The product terms $n_{ph}n_e$ and $n_{ph}n_{ph}$ appearing in Compton scattering and pair production make the problem non-linear and the coupled kinetic equations are solved with the Newton-Raphson method. We have checked that our code is able to properly account for particle cooling as well as to reproduce semi-analytical examples. Those tests are presented in Appendix C.

3 MODEL SETUP: ANALYTICAL ESTIMATION OF MODEL PARAMETERS

The broadband spectrum of blazars extends from radio to the HE or VHE γ -ray bands, covering a large 10^{20} Hz frequency range (e.g., Padovani et al. 2017). The observed nonthermal emission is produced in the jet and can be explained by different models. The primary dichotomy is the split between leptonic and hadronic models, depending on the type of particles (electron-positron pairs or hadrons) initiating the emission. On the one hand, leptonic models are solely based on the synchrotron emission of relativistic electrons at low energy, while the HE peak is explained either by synchrotron self-Compton, hereinafter SSC, or by external Compton process. These models assume that proton emission has a negligible contribution to the overall SED, and therefore lack the ability to produce a significant amount of VHE neutrinos ($\sim 10^{15}$ eV) as detected by the IceCube observatory (IceCube Collaboration 2013; Aartsen et al. 2013). In contrast, the so-called hadronic models assume that protons are also efficiently accelerated in the jet and contribute to the multiwavelength spectrum either by the synchrotron process, or by the radiation from the secondaries produced in photo-pair and photo-pion interactions.

The modeling of the observed SEDs, be it leptonic, hadronic or lepto-hadronic, is a regular approach and is a unique way to investigate the physical processes taking place in jets. The particle spectra are defined by the acceleration and cooling processes within the jet, which may vary from source to source. In this work, we assume that particles are instantaneously accelerated and injected in the emission zone where they radiate their energy. The particle injection spectrum is usually assumed to be a simple power-law, a power-law with an exponential cutoff or a broken power-law. Additionally, the emitting region can contain broad external photon fields which interact with the relativistic particles in the jet. For instance, photons emitted by the dusty torus or reflected by the broad line region play a crucial role in shaping the multiwavelength emission of FSRQs (e.g., order of minutes, Sikora et al. 2009, 1994; Ghisellini & Tavecchio 2009). Moreover an arbitrary distributed photon field can be considered as well, which is necessary for complex scenarios such as the multi-zones or the spine-sheath layer models (Tavecchio & Ghisellini 2008). *SOPRANO* is designed to

work with arbitrary injection particle spectrum as well as arbitrary external photon field, and proceed to compute the evolution of particle spectrum. This makes *SOPRANO* an ideal code to investigate the emission processes in different astrophysical environment.

Within the leptonic and hadronic interpretation of the blazar SEDs, it is assumed that the emission is produced in a spherical blob of comoving size R' that moves towards the observer with a bulk Lorentz factor $\Gamma \sim \delta$, where δ is the Doppler factor. Accelerated leptons and hadrons are injected in the emitting region, which is uniformly filled with a magnetic field of strength B . The magnetic jet luminosity is

$$L_B = \pi c R'^2 \delta^2 \frac{B^2}{8\pi}, \quad (1)$$

where c is the speed of light. We assume that protons are injected in the comoving frame with a power-law spectrum:

$$Q'_p(\gamma_p) = Q'_{0,p} \gamma_p^{-\alpha_p} \quad \gamma_p < \gamma_{p,\max}. \quad (2)$$

The normalization factor $Q'_{0,p}$ is linked to the proton luminosity as

$$L_p = \pi R'^2 \delta^2 m_p c^3 \int \gamma_p Q'_p(\gamma_p) \gamma_p, \quad (3)$$

where m_p is the proton mass. We assume that the injection electron spectrum is given by a power-law with an exponential cut-off :

$$Q'_e(\gamma_e) = \begin{cases} Q'_0 \gamma_e^{-\alpha_e} \exp\left(-\frac{\gamma_e}{\gamma_{e,\text{cut}}}\right) & \gamma_{e,\min} \leq \gamma_e \leq \gamma_{e,\max}, \\ 0 & \text{otherwise,} \end{cases} \quad (4)$$

where $\gamma_{e,\min}$ is the minimum injection Lorentz factor. The electron luminosity is then given by

$$L_e = \pi R'^2 \delta^2 m_e c^3 \int \gamma_e Q'_e(\gamma_e) d\gamma_e, \quad (5)$$

where m_e is the electron mass. In general $\gamma_{e,\text{cut}}$ should be defined by the equality of the acceleration and cooling time-scales. However, in order to have a broad inference of the physical processes in the jet, $\gamma_{e,\text{cut}}$ is considered a free parameter which will be constrained by the data. The distribution functions of protons and electrons evolve via cooling and via interaction with photons, producing different signatures in the broadband spectrum. Our aim is to identify those signatures and use them to constrain the emission mechanism within the framework of different scenarios.

In one dynamical time-scale, $t'_d \sim R'/c$, electrons and positrons cool to Lorentz factor

$$\gamma_{e,c} = \frac{6\pi m_e c^2}{B^2 R' \sigma_T} \sim 2.3 \times 10^3 B^{-2} R'^{-1}_{16}, \quad (6)$$

where σ_T is the Thompson cross-section. The associated observed synchrotron characteristic frequency is

$$\nu_{e,c} = \frac{48\pi \delta c^3 m_e q}{B^3 R'^2 \sigma_T^2} \sim 4.0 \times 10^{14} \delta_1 B^{-3} R'^{-2}_{16} \text{ Hz}, \quad (7)$$

where q is the elementary charge. The frequency $\nu_{e,c}$ is usually associated to the peak frequency of the low energy component in the SED. The injection frequency corresponding to electrons with Lorentz factor $\gamma_{e,\min}$ is given by

$$\nu_{e,m} = \frac{4}{3\pi} \frac{q B \delta \gamma_{e,\min}^2}{m_e c} \sim 7.5 \times 10^{15} B_0 \delta_1 \gamma_{e,\min,4}^2 \text{ Hz}. \quad (8)$$

Another turnover in the synchrotron spectrum is at the self-absorption frequency ν_{SSA} . Synchrotron self-absorption dominates at low frequency, specifically in the radio band, and introduces a cut-off

like modification around the frequency ν_{SSA} (Nalewajko et al. 2014):

$$\nu'_{\text{SSA}} \approx \frac{1}{3} \left(\frac{e B'}{m_e^2 c} \right)^{1/7} \frac{L_{\text{syn}}^{2/7}}{R'^{4/7}} \quad (9)$$

where L'_{syn} is the synchrotron energy distribution peak luminosity.

The interaction between the photons of the low energy hump and the electrons and positrons producing this hump via synchrotron radiation can produce the second peak in the broadband spectrum (SSC). The peak frequency of this component depends on the cooling regime of the electrons and on the peak frequency of the synchrotron component. It is given by

$$\nu_{\text{IC}} = \begin{cases} 2\gamma_{e,\min}^2 \nu_{e,m} & \nu_{e,c} < \nu_{e,m} \\ 2\gamma_{e,c}^2 \nu_{e,c} & \nu_{e,m} < \nu_{e,c} \end{cases} \sim \begin{cases} 1.5 \times 10^{24} B \delta_1 \gamma_{e,\min,4}^4 \text{ Hz}, & \nu_{e,c} < \nu_{e,m} \\ 4.3 \times 10^{21} \delta_1 B^{-7} R'^4_{16} \text{ Hz}, & \nu_{e,m} < \nu_{e,c} \end{cases} \quad (10)$$

for fast and slow cooling respectively. Similarly, the ratio of luminosities of the synchrotron L_s and the inverse self-Compton L_{IC} components can be approximated by

$$\frac{L_{\text{SSC}}}{L_{\text{syn}}} \sim \begin{cases} \frac{2}{3} \tau \gamma_{e,c}^2 \left(\frac{\gamma_{e,c}}{\gamma_{e,\min}} \right)^{1-\alpha_e} & \nu_{e,c} > \nu_{e,m} \\ \frac{2}{3} \tau \gamma_{e,c} \gamma_{e,\min} & \nu_{e,c} < \nu_{e,m} \end{cases} \quad (11)$$

where $\tau = \sigma_T R' n'_e$ is the opacity of the source for the Compton process and n'_e is the comoving electron density. It is computed assuming that the Thomson regime is achieved for the peak, which might not always be the case.

For hadronic models (hereinafter HM), and more specifically for proton synchrotron models, the HE component of the SED is dominated by the proton synchrotron radiation rather than by the inverse Compton scattering. This model requires that a substantial number of protons are accelerated in the jet to very large Lorentz factor². In this case, the required magnetic field is larger than in leptonic models, with B in the order of hundred Gauss. The peak frequency of proton synchrotron emission is at:

$$\nu_s^p = 4.1 \times 10^{24} B_2 \delta_1 \gamma_{p,\max,9}^2 \text{ Hz}, \quad (12)$$

where we did not consider cooling. In general, hadronic models necessitate much more energetic jets since they require a large magnetic field, as well as a significant amount of energy in relativistic protons. We further discuss these constraints in Section 5. In addition to synchrotron losses, relativistic protons of the jet also lose energy by photo-pion and Bethe-Heitler photo-pair interactions with the photons.

For hybrid models, a subclass of hadronic models, the low and high energy peaks are explained by leptonic processes and proton synchrotron emission is required to be subdominant. The requirement on proton content is obtained by maximizing the neutrino flux at PeV energies, which is constrained by the radiation from the secondaries produced by the Bethe-Heitler and photo-pion processes. Indeed, it has long been speculated that efficient neutrino production is associated with efficient Bethe-Heitler

² In principle, the maximum proton energy γ_p could be estimated by assuming an acceleration time of the form $t_{\text{acc}} \sim \gamma_p m_p c^2 / (\eta q B)$, where $\eta \sim 1$ is the acceleration efficiency. This time is then compared to the different cooling time scale to obtain an estimate of $\gamma_{p,\max}$.

process, creating a population of HE pairs, which can over-shine the tight constraints in the X-ray band (e.g., order of minutes, [Petropoulou & Mastichiadis 2015](#)).

In order to produce PeV neutrinos, protons should have a comoving energy larger than $E'_p > 10^{15}/\delta_1$ eV. Assuming for simplicity that the Bethe-Heitler process creates pairs with Lorentz factor $\gamma_{\pm} = \gamma_p/5^3$, the pairs created by the protons producing PeV neutrinos are in the fast cooling regime, see Equation (6). Therefore, the energy produced in the Bethe-Heitler process is efficiently radiated by synchrotron radiation. For an electron or positron to radiate in X-ray, its Lorentz factor should be

$$\gamma_{\pm}^{\text{1keV}} = \sqrt{\frac{3\pi v c m_e}{4B\delta q_e}} \sim 5.7 \times 10^3 v_{\text{1keV}}^{\frac{1}{2}} B_2^{-\frac{1}{2}} \delta_1^{-\frac{1}{2}}. \quad (13)$$

which is smaller than the Lorentz factor of the pairs from the protons producing PeV neutrinos. Therefore, synchrotron radiation from the Bethe-Heitler pairs contributes to the X-ray band. We now estimate the Bethe-Heitler pair spectrum. The Bethe-Heitler pair yield is

$$\frac{dn_{\pm}}{dt}(\gamma_{\pm}) = 2c \int_0^{\infty} dx n_{\text{ph}}(x) \int_1^{\infty} d\gamma_p N_p \frac{d\sigma_{\pm}}{d\gamma_{\pm}}. \quad (14)$$

where $x = h\nu/(m_e c^2)$ is the photon energy normalised to the electron rest mass. Under the head-on approximation and if the photon energy is small enough to neglect proton recoil, the differential pair rate can be written as ([Crumley & Kumar 2013](#))

$$\frac{d\sigma_{\pm}}{d\gamma_{\pm}} \sim \frac{\alpha\sigma_T}{2x\gamma_{\pm}^2} \quad \frac{1}{2x} \leq \gamma_{\pm} \leq \frac{\gamma_p}{2}, \quad (15)$$

where α is the fine structure constant. We further assume that the photon spectrum is well approximated by $n_{\gamma}(\epsilon) = n_{\gamma,0}\epsilon^{-\alpha_{\text{ph}}}$, which is realistic since the synchrotron emission from the electrons forming the low energy bump can be well approximated by a succession of power-laws with indexes $\alpha_{\text{ph}} = 2/3, 3/2, (\alpha_e + 1)/2$, where we neglected self-absorption and specialised to the fast cooling scenario, usually appropriate for HM. We also further assume that protons do not cool substantially such that their distribution function is $N_p = N_{p,0}\gamma_p^{-\alpha_p}$ for $\gamma_p < \gamma_{p,\text{max}}$, then the integral of Equation 14 yields

$$\frac{dn_{\pm}}{dt}(\gamma_{\pm}) \simeq \alpha c \sigma_T 2^{\alpha_{\text{ph}}+2-\alpha_p} \frac{n_0}{\alpha_{\text{ph}} \alpha_p - 1} \frac{N_0}{\gamma_{\pm}^{\alpha_{\text{ph}}-\alpha_p-1}} \quad (16)$$

Therefore, the pair injection spectrum will be formed of three smoothly connected power-laws with indexes $\alpha_{\text{ph}} - \alpha_p - 1$, where $\alpha_{\text{ph}} = 2/3, 3/2, (\alpha_e + 1)/2$. Since these pairs are in the fast cooling regime, their distribution function is well approximated by smoothly connected power-laws with indexes $q = \alpha_{\text{ph}} - \alpha_p - 2$. From [Rybicki & Lightman \(1979\)](#), the resulting photon flux is well approximated by three smoothly connected power-laws $F_{\nu} \propto \nu^{-q/2}$.

In proton synchrotron models, when the proton injection index is $\alpha_p \sim 2$, the specific spectral power νF_{ν} of the synchrotron emission from the Bethe-Heitler pairs is nearly flat with indexes $-2/3, -1/4, -(\alpha_e - 3)/4$. The spectrum extends up to energies

$$\nu_{\pm,\text{max}} \sim \left(\frac{\gamma_{\pm}}{\gamma_{p,\text{max}}} \right)^2 \frac{m_p}{m_e} v_s^p \sim 3.0 \times 10^{26} B_2 \delta_1 \gamma_{p,9}^2 \text{ Hz}. \quad (17)$$

where we used Equation (12) for the synchrotron frequency associated to the highest energy protons with Lorentz factor $\gamma_{p,\text{max}}$. Yet, because the pair synchrotron emission peaks at such a large

frequency, its contribution to the X-ray is likely to be small and not constraining for proton synchrotron models. However, this is not the case for hybrid models when the peak frequency for synchrotron radiation from the pairs will be

$$\nu_{\pm,\text{max}} \sim 3.0 \times 10^{19} B_{-1} \delta_1 \gamma_{p,7}^2 \text{ Hz}, \quad (18)$$

around the X-ray frequency, in agreement with the estimates from [Petropoulou & Mastichiadis \(2015\)](#). It is clear that increasing the neutrino flux requires to increase the density of protons or of photons. This leads to an increase of the production rate of pairs, and as a result, a larger synchrotron flux in the X-ray band, which becomes critical for constraining this type of models ([Petropoulou & Mastichiadis 2015](#); [Gao et al. 2019a](#); [Reimer et al. 2019](#)).

4 MODELING OF BLAZAR SEDS

The code *SOPRANO*, described in Section 2, is used to model the multiwavelength SEDs of TXS 0506+056, 3HSP J095507.9+355101 and 3C 279. Two of these sources, TXS 0506+056 and 3HSP J095507.9+355101, coincide in space and time with the IceCube 170922A and IceCube 200107A events, respectively. The other source, 3C 279, shows a prominent flare in the γ -ray band.

It is assumed that protons and electrons are injected in the emitting region with energy distributions given by Equations (2) and (4), respectively. We also assume that the injection power-law indexes are such that $\alpha_e = \alpha_p$. Once injected in the emitting region, particles interact with the magnetic field and with the photons, producing secondary particles, which themselves interact, radiate and decay, shaping the broadband SED. The low energy component is interpreted as the synchrotron emission of the primary electrons while the HE component is formed by joint contributions of inverse Compton scattering of primary electrons and of synchrotron radiation from the protons, as well as secondary particles from photo-hadronic interactions. The system of kinetic equations is evolved for one dynamical time scale $t'_{\text{dyn}} \sim R'/c$ considering the magnetic field to be constant, and taking into account all relevant processes for particles interactions.

4.1 Modeling of TXS 0506+056 SED

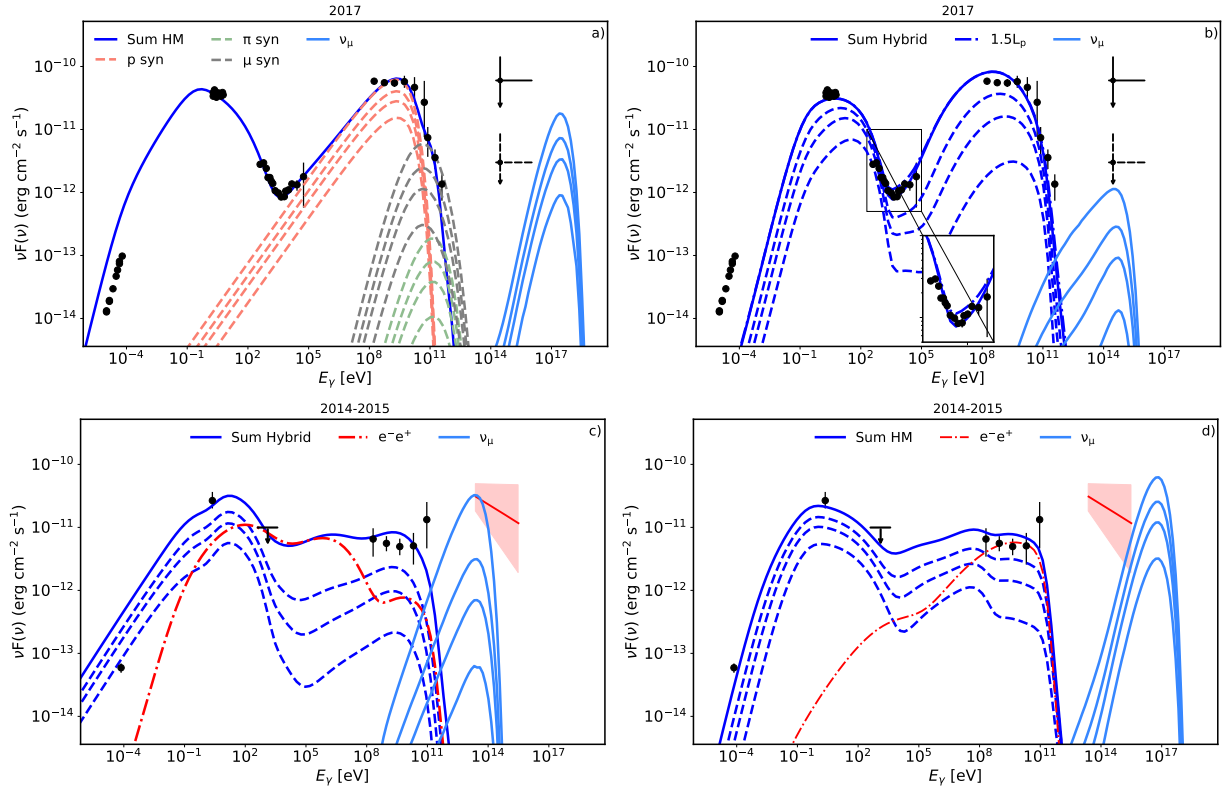
After the observations of neutrinos from the direction of TXS 0506+056 ([IceCube Collaboration et al. 2018a,b](#)), hadronic processes in its jet have been extensively studied. The multiwavelength emission and neutrino production were discussed for the $p\gamma$ ([Ansoldi et al. 2018](#); [Keivani et al. 2018b](#); [Murase et al. 2018](#); [Cerruti et al. 2019a](#); [Gao et al. 2019b](#); [Righi et al. 2019](#); [Petropoulou et al. 2020a](#)) and pp ([Sahakyan 2018](#); [Liu et al. 2019](#)) interaction scenarios. The current modeling consensus is that the applied one zone models predict, albeit low, but still consistent results with the observation of one neutrino event in 2017. However, the neutrino flare in 2014–2015 cannot be explained when both the neutrinos and the electromagnetic emission are produced from the same region.

Panels a) and b) of Figure 1 show the SED of TXS 0506+056 when the neutrino event was observed. The multiwavelength data from [IceCube Collaboration et al. \(2018a\)](#) are modeled within a HM scenario in panel a). The corresponding model parameters are given in Table 1. The sum of all components, represented by the blue line in the top left panel of Figure 1, satisfactorily explains the observed data. The model over-predicts the radio data, but when taking the synchrotron self-absorption into account via Equation (9), which is significant below the energies $\approx 10^{-3}$ eV ($\approx 3 \times$

³ This assumption requires the inelasticity to be $\kappa_e \sim 10^{-4}$. [Mastichiadis et al. \(2005\)](#) computed the inelasticity and finds that it steadily decreases from 10^{-3} for increasing $\gamma_p x$, where $x = h\nu/(m_e c^2)$, with h the Planck constant.

Table 1. Parameter sets used for modeling the SEDs of TXS 0506+056, observed in 2017 and during the neutrino flare in 2014-2015. The electron, proton and magnetic luminosities are also given.

TXS 0506+056				
	2017		2014-2015	
	Hadronic	Lepto-hadronic	Hadronic	Lepto-hadronic
δ	20	20	15	10
$R/10^{15}$ cm	2.5	10	1	100
$B[G]$	80	0.57	35	0.65
$\gamma_{e,min}$	100	1000	2×10^2	9×10^3
$\gamma_{e,cut}$	2.4×10^3	4.5×10^4	10^4	$=\gamma_{e,max}$
$\gamma_{e,max}$	3×10^4	6×10^4	8×10^4	8×10^4
α_e	2.1	2.0	2.0	2.0
$\alpha_p = \alpha_e$	2.1	2.0	2.0	2.0
$\gamma_{p,min}$	1	1	1	1
$\gamma_{p,max}$	10^9	10^6	2×10^8	1.2×10^5
L_e (erg s $^{-1}$)	2.2×10^{44}	9.3×10^{44}	2.8×10^{44}	5.3×10^{44}
L_B (erg s $^{-1}$)	6.0×10^{46}	4.9×10^{43}	10^{45}	1.6×10^{45}
L_p (erg s $^{-1}$)	2.1×10^{47}	2.6×10^{50}	3.4×10^{47}	4.9×10^{52}

**Figure 1.** The multiwavelength SED of TXS 0506+056 during the neutrino emission in 2017 (upper panels) and during the neutrino flare in 2014-2015 (lower panels) modeled within the hadronic and lepto-hadronic hybrid scenarios. The solid blue line in all plots represents the sum of all components which has been corrected for EBL absorption considering the model of Domínguez et al. (2011).

10^{11} Hz) the model is in agreement with the data. Under the guise of our modeling, the data up to the soft X-ray band are produced by synchrotron emission of electrons, which are in the fast-cooling regime. Indeed the magnetic field is required to be high, $B = 80$ G, to explain the HE peak with proton synchrotron emission, shown by the red dashed line in panel a) of Figure 1, with a contribution of muon synchrotron emission at HEs, represented by the gray dashed line. The contribution of pion synchrotron emission is negligible and

does not contribute substantially to the flux observed by the MAGIC telescopes (Ansoldi et al. 2018). The emission in the transition region between the low and high energy components, in the X-ray band, is dominated by proton synchrotron emission, with little contribution from the cascade emission of the secondary pairs produced from the absorption of VHE γ -rays and by the emission of pairs from the Bethe-Heitler process.

The modeling parameters given in the first column of Table 1

are in the range of similar estimations for blazars in general and for TXS 0506+056 in particular. A Doppler factor $\delta = 20$ and a radius $R' = 2.5 \times 10^{15}$ cm were used in our modeling. This is in agreement with the limits on the variability time of 10^5 s presented in [Keivani et al. \(2018a\)](#) and in [Padovani et al. \(2019\)](#). We note that when $\delta = 10$ or 15, the data can also be well reproduced by the model. The radius, which defines the density of interacting particles and photons, is a crucial quantity in defining the type of model. The initial injection power-law index of the emitting electrons is $\alpha_e = 2.1$, a value that can be formed by shock accelerations, *e.g.* [Blandford & Eichler \(1987\)](#). Due to the high magnetic field, $B = 80$ G, electrons are in the fast cooling regime and their distribution function is a power-law with index $\alpha_e + 1$. The initial electron distribution extends up to $\gamma_{\text{cut}} = 2.4 \times 10^3$ (~ 1 GeV) which is representative of the acceleration and cooling time scales. Instead, protons cool less efficiently and they could be accelerated up to much higher energies, *i.e.* $\gamma_{\text{max}} = 10^9$ (9.4×10^{17} eV), see the discussion in Section 5.

Previous modelings of TXS 0506+056 have shown that hybrid models can be good alternatives to proton synchrotron or leptonic models ([Cerruti et al. 2019a](#); [Gao et al. 2019a](#)). They are found to be favourable from the point of view of neutrino observations. The SED of TXS 0506+056, now modeled within the framework of a hybrid lepto-hadronic scenario, is shown in panel b) of Figure 1. The model parameters are given in the second column of Table 1. The blue dashed lines represent the time evolution of the spectrum in selected numerical steps, which builds and forms the overall SED, represented by the solid blue line after one dynamical time scale.

The synchrotron component peaking between 1-10 eV is up-scattered by the relativistic electrons to produce the HE and VHE component. The magnetic field in the emitting region is $B = 0.57$ G significantly lower than for the proton synchrotron modeling. Therefore, electrons with Lorentz factor $\gamma_{e,\text{min}} = 10^3$ are not substantially cooled in one dynamical time scale. The electron distribution function is a broken power-law with an exponential cut-off, $\gamma_e^{-\alpha_e}$ and $\gamma_e^{-\alpha_e+1} \exp[-\gamma_e/\gamma_{e,\text{cut}}]$, with a break at Lorentz factor $\gamma_{e,c} = 7 \times 10^3$, where we used Equation (6). In order for the neutrino spectrum to peak around the energy of the observed neutrino (290 TeV), the comoving proton distribution function should extend at least up to $\gamma_{p,\text{max}} = 10^6 \delta_1^{-1}$. This Lorentz factor is lower than what is usually used in pure HM models. For this hybrid model, protons do not directly contribute to the observed SED. Their radiative signature is due to the emission of the secondaries of photo-pion and photo-pair interactions. Their contribution dominates in the X-ray band, which constrains the proton luminosity and as a consequence the neutrino luminosity. For example, if one increases by 1.5 times the proton luminosity, the model would overshoot the X-ray data, as shown by the dotted-dashed blue line in panel b) of Figure 1.

We now present our results of the SED modeling obtained during the historical neutrino flare of TXS 0506+056. Unfortunately, when 13 ± 5 neutrinos were observed between October 2014 and March 2015 ([IceCube Collaboration et al. 2018b](#)), the multiwavelength coverage is scarce. Yet, the flux upper limit of $F < 9.12 \times 10^{-12}$ erg cm $^{-2}$ s $^{-1}$ derived from Swift BAT observations ([Reimer et al. 2019](#)) introduces substantial difficulties for a one-zone modeling. Indeed, the predicted number of neutrino events cannot be matched to the IceCube observations. [Reimer et al. \(2019\)](#) and [Rodrigues et al. \(2019\)](#) have shown that only few neutrino events could be detected under different optimistic considerations for the emitting region and for the target photon field (internal or external to the jet). Matching together the observed multiwavelength data and the neutrino data seems to require two zone models with more free parameters ([Reimer et al. 2019](#); [Rodrigues et al. 2019](#)).

To accommodate the X-ray limit and try to account for the neutrino flux during this flare, two different assumptions on the proton distribution function are made. On the one hand, radiation from the secondaries can be constrained to be dominant in the MeV band, in which there are no observational constraint. On the other hand, radiation from the secondaries could be dominant in the GeV band and produce the second HE hump. The SEDs of these two models are respectively shown in panels c) and d) of Figure 1, with data from [Rodrigues et al. \(2019\)](#). Those two models lead to two very different sets of parameters for the emitting region, see column 3 and 4 of Table 1. The first model requires a large radius $R' = 10^{17}$ cm and a slowly moving jet with Doppler factor $\delta = 10$, while the second model necessitates those parameters to be $R' = 10^{15}$ cm and $\delta = 15$. The required magnetic field also significantly differs between these two models with $B = 35$ G for the first model, to be compared to $B = 0.65$ G for the second one. The first model tends to reproduce the neutrino flux, albeit produces the peak at lower energies. The second model puts the neutrino peak at larger energy, but is not able to reproduce the observed neutrino number. In both interpretations, it is clear that the upper limit in the X-ray band imposes strong constraints on the photon spectrum, which in turn limits the proton content in the jet. Considering larger proton luminosity would lead to over-estimate both the observed γ -ray flux and the X-ray upper limit.

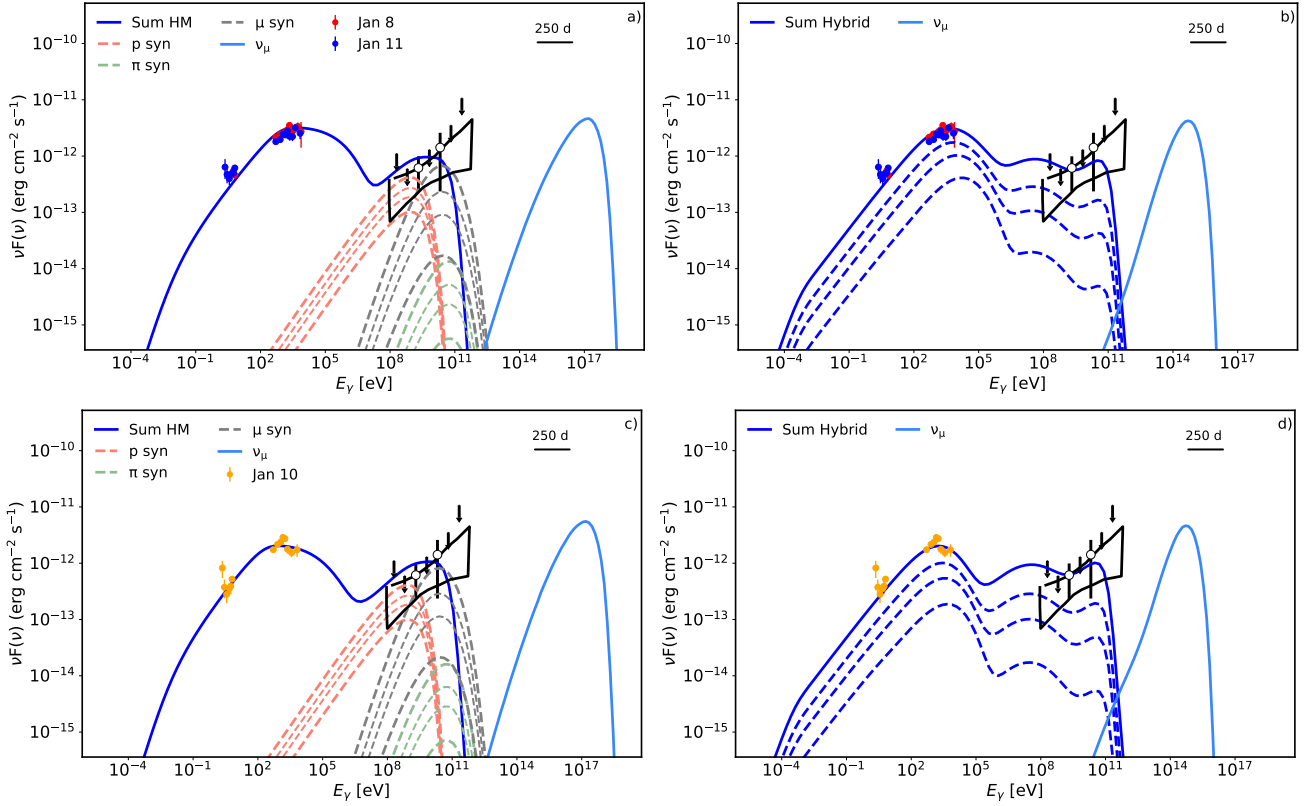
4.2 Modeling of 3HSP J095507.9+355101 SED

The blazar 3HSP J095507.9+355101 is another interesting source to study within a hadronic scenario. Indeed, it is a nearby blazar at redshift $z = 0.55703$ ([Paiano et al. 2020](#)), and it lies in the error region of the neutrino event IC 200107A ([Giommi et al. 2020b](#)). The multiwavelength campaign, which started after the neutrino detection in January 2020, showed that 3HSP J095507.9+355101 was in a bright X-ray emission state with a synchrotron peak frequency of 5×10^{17} Hz ([Giommi et al. 2020a](#)). This is a typical value for extreme peak blazars ([Costamante et al. 2001](#)). It is the first time that the jet of an extreme blazar is associated with a neutrino event, straightening the assumption that the jets of this blazar type are potential sites for cosmic rays and even ultra-high energy cosmic ray acceleration ([Padovani et al. 2016](#)). The multimessenger emission from 3HSP J095507.9+355101 was interpreted within various leptonic and lepto-hadronic models by [Petropoulou et al. \(2020b\)](#) and [Paliya et al. \(2020\)](#). [Petropoulou et al. \(2020b\)](#) showed that a change of the X-ray flux above 1 keV does not significantly affect the neutrino flux. The expected number of neutrinos during the 44-day period is 6×10^{-4} with a low probability of ~ 0.06 % to detect one or more neutrinos. Alternatively, [Paliya et al. \(2020\)](#) investigated the effects of the external photon fields to enhance the neutrino production.

The SED of 3HSP J095507.9+355101 is shown in Figure 2, where the multiwavelength data are from [Giommi et al. \(2020a\)](#). Optical, UV and X-ray data were acquired on the 8th, 10th and 11th of January. However, since the data taken on the 8th and 11th of January seem to have the same flux and spectral shape ([Petropoulou et al. 2020b](#)), we only model the data from the 8th. The lack of available multiwavelength data does not allow to constrain the low and high energy peaks, which hardens the estimation of the model free parameters. A hint of a 20 – 30 minutes variability has been found in the NICER and NuSTAR data, but only at the $\sim 3.5 \sigma$ level ([Paliya et al. 2020](#)). Therefore, the compactness of the emitting region cannot be constrained. [Petropoulou et al. \(2020b\)](#) investigated the blob radius–Doppler factor relation for a wide range of photo-pion production efficiency and for several set of parameters. In order to keep the generality, in the current study, the SED of

Table 2. Parameters used to model the multiwavelength SEDs of 3HSP J095507.9+355101 and 3C 279. The electron, proton and magnetic luminosity is also displayed.

	3HSP J095507.9+355101		3C 279	
	January 8th		January 10th	
	Hadronic	Lepto-hadronic	Hadronic	Lepto-hadronic
δ	15	30	15	30
$R/10^{15}$ cm	0.3	10	0.3	10
$B[G]$	45	0.11	45	0.08
$\gamma_{e,min}$	10^4	100	5×10^3	100
$\gamma_{e,cut}$	6×10^5	2×10^6	2×10^5	7×10^5
$\gamma_{e,max}$	9×10^5	6×10^6	5×10^5	6×10^6
α_e	1.9	2.0	1.9	2
$\alpha_p = \alpha_e$	1.9	2.0	1.9	2
$\gamma_{p,min}$	1	1	1	1
$\gamma_{p,max}$	9×10^8	10^6	9×10^8	10^6
L_e (erg s $^{-1}$)	1.2×10^{44}	1.6×10^{44}	7.3×10^{43}	2.1×10^{44}
L_B (erg s $^{-1}$)	1.5×10^{44}	4.1×10^{42}	1.5×10^{44}	2.2×10^{42}
L_p (erg s $^{-1}$)	3.2×10^{46}	8.0×10^{50}	3.2×10^{46}	1.8×10^{51}

**Figure 2.** The multiwavelength SEDs of 3HSP J095507.9+355101 on the 8th and 11th of January (panels a) and b) on the top row) and on the 10th of January (panels c) and d) on the bottom row). The data are taken from [Giommi et al. \(2020a\)](#); [Petropoulou et al. \(2020b\)](#). The observed spectrum including all processes is shown by the solid blue line. All models (solid blue lines) have been corrected for EBL absorption considering the model of [Domínguez et al. \(2011\)](#).

3HSP J095507.9+355101 is modeled for two different parameter configurations. For the HM, we consider $R' = 3 \times 10^{14}$ cm and $\delta = 15$, while for the lepto-hadronic model we assume $R' \approx 10^{16}$ cm and $\delta = 30$.

In our hadronic modeling, the HE component is mainly due to the synchrotron emission of protons, shown by the red dashed line

in panel a) of Figure 2. Protons are assumed to have an energy distribution $N_p \propto \gamma_p^{-1.9}$ and to be accelerated up to $\gamma_{p,max} = 9 \times 10^8$, corresponding to 8.4×10^{17} eV. At VHEs, the largest contribution is due to muon synchrotron radiation, represented by the gray dashed line in panel a) of Figure 2. The high synchrotron peak at $\sim 10^4$ eV can be reproduced when $\gamma_{e,cut} = 6 \times 10^5$ and $B = 45$ G. The minimal

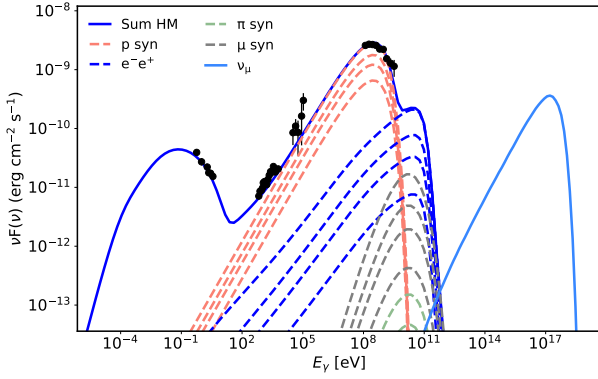


Figure 3. The multiwavelength SED of 3C 279 during the exceptional flaring activity in 2015. The contribution of different particle emission is shown by dashed lines whereas the thick solid line represents the observed spectrum, corrected for EBL absorption considering the model of Domínguez et al. (2011).

energy of the accelerated electrons is relatively high, $\gamma_{e,\min} = 10^4$, but still in the range of parameters usually estimated for ultra-high-frequency-peaked blazars, see e.g. Cerruti et al. (2015b). For the hybrid lepto-hadronic modeling, shown in panel b) of Figure 2, the emitting electrons should be accelerated up to $\gamma_{e,\text{cut}} = 2 \times 10^6$ so the SSC component extends to the GeV band to explain the observed data. In this model, a lower magnetic field of 0.11 G is required because of the larger radius of the emitting region ($R' = 10^{16}$ cm). The emission of the secondary pairs from protons accelerated up to $\gamma_{p,\max} = 10^6$ dominates in the sub-MeV band.

The hadronic and hybrid modeling of the SED observed on the 10th of January 2020, is displayed in panel c) and d) of Figure 2, respectively. Since the peak of the low energy component, defined by the X-ray data, is at lower energies than for observations performed on the 8th of January, the modeling requires a three times smaller cutoff energy, i.e. $\gamma_{e,\text{cut}} = 2 \times 10^5$ and $\gamma_{e,\text{cut}} = 7 \times 10^5$ for the hadronic and lepto-hadronic modelings, respectively. The other parameters are given in Table 2 and are similar with these obtained from modeling the data observed on the 8th of January.

4.3 Modeling of 3C 279 SED during the 2015 flare

The emission from the powerful FSRQs 3C 279 at redshift $z = 0.536$ has been detected in all possible spectral bands. Its broadband emission is characterized by high amplitude variability almost in all energy bands (e.g., order of minutes, Aleksić et al. 2014b) and in particular in the HE γ -ray band, which present the fastest variability. On the 16th of June 2015, Fermi LAT observations showed that 3C 279 was in an exceptionally bright state. The flux increased up to 3.6×10^{-5} photon $\text{cm}^{-2} \text{s}^{-1}$ with a flux doubling time on the order of 5 minutes (Ackermann et al. 2016). IceCube performed a time-dependent neutrino signal search correlated with this γ -ray flare but no evidence for a signal was found (Abbasi et al. 2021). We use SOPRANO to model the SED of 3C 279 during its flare to infer the neutrino flux. We consider a HM and explain the second peak with proton synchrotron emission. The parameters of our modeling are given in Table 2.

Figure 3 shows the multiwavelength SED of 3C 279 taken from Bottacini et al. (2016), alongside with the results of our modeling. During the brightening, the X-ray emission of the source appears with a hard photon index < 1.50 , smoothly connecting with the INTEGRAL data, described by a power-law with index

1.08 (Bottacini et al. 2016). In the HE γ -ray band, the spectrum presents a power-law with photon index 2.21 with a turn over (Paliya 2015). We make the hypothesis that the HE component is produced from a single mechanism. In our modeling it is interpreted as proton synchrotron emission, represented by the red dashed lines in Figure 3. This interpretation requires that protons are accelerated up to $\gamma_{p,\max} = 2.1 \times 10^8$, see Table 2. The compactness of the emitting region implies a high efficiency for photo-pion and photo-pair interactions, which inject energetic secondary pairs. The contribution of these pairs dominates above ~ 10 GeV and peak at ~ 100 GeV, as can be seen by the blue dashed line in Figure 3. The synchrotron radiation of the primary electrons peaks at ~ 0.1 eV and its HE tail accounts for the observed optical/UV data. These data constrain the cut-off energy to be relatively low, $\gamma_{e,\text{cut}} = 2.4 \times 10^2$, otherwise, for $B = 70$ G and $\delta = 55$, the synchrotron radiation would overshoot the observed flux in optical and UV bands. A similar hadronic modeling for this flare is presented in Bottacini et al. (2016) and in Petropoulou et al. (2017).

5 DISCUSSION

The primary class of objects to be studied in the multimessenger context are blazars which are associated with neutrino events observed by IceCube. Even if the associations are not at the 5σ significance level, the observations by IceCube put some constraints on the physical processes taking place in relativistic jets. Using the hadronic time-dependent model constrained by their neutrino emission, the broadband SEDs of two blazars, namely TXS 0506+056 and 3HSP J095507.9+355101, respectively associated to the neutrino events IC 170922A and IC 200107A, are studied. We also analysed the SED of 3C 279 during its 2015 γ -ray flaring period. For each source, we present several modelings assuming that different components dominate in the HE γ -ray band. For the sources studied in this paper, we find that the proton synchrotron model, the secondaries emission model and the hybrid lepto-hadronic model can explain the observed SEDs under sensible assumptions for the particle energy distributions.

Some of our modelings require a compact emitting region, with $R' \lesssim 10^{15}$ cm. In principle, the maximum energy of the particles, and specifically of the protons, is limited by requiring their Larmor radius, given by $r_{p,L} = \gamma_p m_p c^2 / (qB)$, to be smaller than the emission region. All our models are consistent with this requirement, and therefore protons can be accelerated to the maximum energy as given in Tables 1 and 2. The strongest constraints are obtained for the hadronic model of 3HSP J095507.9+355101 for which the protons with $\gamma_{p,\max} = 9 \times 10^8$ have Larmor radius $r_L = 6.3 \times 10^{13}$ cm, while the emitting region has size $R = 3 \times 10^{14}$ cm. The maximum particle energy can also be limited by synchrotron cooling. Specifically, de Jager et al. (1996) balanced acceleration time-scales for shock and gyroresonant acceleration with cooling time scale via the synchrotron process to find that the electrons can be accelerated up to

$$\gamma_e^{\max} \sim 4 \times 10^7 B^{-\frac{1}{2}}. \quad (19)$$

For all our modelings, we have $\gamma_{e,\max} < \gamma_e^{\max}$. Only the lepto-hadronic modeling of 3HSP J095507.9+355101 is marginally consistent with this limit. Such constraints are highly dependent on the acceleration mechanism and vary for alternative scenarios, such as particle acceleration by magnetic reconnection or in shear layers.

The power-law index of the accelerated particles, assumed to be equal for protons and electrons, is found to be in the range $\alpha = 1.8 - 2.1$, a value in agreement with prediction of shock

acceleration theories (e.g., order of minutes, Kirk et al. 2000; Summerlin & Baring 2012). This index is defined by the acceleration processes, and we note that protons and electrons could have different indexes. In fact, if particles are accelerated by shocks, the properties of their acceleration depend on the direction of the shock with the magnetic field: quasi-parallel shocks accelerate both ions and electrons, while quasi-perpendicular shocks only accelerate electrons (Caprioli & Spitkovsky 2014a,b,c; Park et al. 2015; Guo et al. 2014). It is worth noting that magnetic reconnection could be the mechanism accelerating particles in blazar jets, see e.g. Giannios & Uzdensky (2019), in which case it is also expected that the power-law of accelerated electrons and protons be slightly different (e.g., order of minutes, Guo et al. 2016)).

An important quantity allowing to compare and contrast the models is the luminosity carried out by electrons, protons and the magnetic field. They are respectively computed with Equations (1), (3) and (5) and are given in Table 1 for TXS 0506+056 and Table 2 for 3HSP J095507.9+355101 and 3C 279. In all our models, the total luminosity of the jet is defined by the proton content. This is expected since our models are designed to produce a high neutrino flux. Specifically, in the case of TXS 0506+056, for the proton synchrotron model, shown on panel a) of Figure 1, the required luminosity for the jet is $L_{\text{tot}} = L_p + L_e + L_B = 2.7 \times 10^{47} \text{ erg s}^{-1}$. The energy budget in the emitting region is dominated by the particles $(L_p + L_e)/L_B \approx 3.5$, yet the system is closed to equipartition. For this model, the required luminosity exceeds by one order of magnitude the Eddington luminosity of $\approx 4 \times 10^{46} \text{ erg s}^{-1}$ for a black hole mass of $3 \times 10^8 M_\odot$, as estimated for TXS 0506+056 using the absolute R-band magnitude (Padovani et al. 2019). This is in agreement with previous studies suggesting that in the case of proton synchrotron models or models producing a high neutrino flux, the required jet luminosity exceeds that of the Eddington limit (Xue et al. 2019a). Within a lepto-hadronic model, matching the neutrino flux with the neutrino event of TXS 0506+056, displayed on panel b) of Figure 1, requires the jet luminosity to be $\sim 10^{50} \text{ erg s}^{-1}$, significantly exceeding that of the Eddington luminosity. Although the Eddington luminosity is not a strict limit and super-Eddington luminosities were previously reported (Jiang et al. 2019), this value is extremely large. On the other hand, for the neutrino flare in 2014-2015, when assuming that the emission from the secondary pairs solely dominates in the X-ray and γ -ray bands, an unrealistically high luminosity of $\sim 10^{52} \text{ erg s}^{-1}$ is obtained. Indeed, matching the high neutrino flux with the large radius (10^{17} cm) imposed by the modeling in this case, requires a large protons density, hence the too large proton luminosity. In the alternative interpretation, when the emission from the secondary pairs dominates in the GeV band, a modest luminosity of $3.4 \times 10^{47} \text{ erg s}^{-1}$ is estimated.

For 3HSP J095507.9+355101, the situation is identical to that of TXS 0506+056. For the HM, a luminosity of $3.2 \times 10^{46} \text{ erg s}^{-1}$ is estimated while the lepto-hadronic modeling requires the jet luminosity to be $\sim 10^{51} \text{ erg s}^{-1}$. The black hole mass of 3HSP J095507.9+355101 was estimated, using two different methods, to be $3 \times 10^8 M_\odot$ (Paiano et al. 2020) or $\sim 8 \times 10^8 M_\odot$ (Paliya et al. 2020). Therefore, the luminosity estimated from the hadronic modeling is compatible with the Eddington luminosity $(4 - 10) \times 10^{46} \text{ erg s}^{-1}$. In principle, the proton contribution to the overall jet luminosity can be decreased by assuming that protons have a softer energy distribution, $\alpha_p > 2.0$, different than that of the electrons. However, this introduces a new free parameter for the modeling, and the difference for the proton luminosity would only be a factor of a few.

For 3C 279, the hadronic interpretation of the SED observed in 2015 is natural, considering the difficulties encountered by

the leptonic models. Indeed, when considering external inverse Compton scenario, the interpretation of the observed large Compton dominance (~ 70 , the luminosity ratio of the high- and low -energy components) requires a strongly matter dominated jet (Asano & Hayashida 2015). In the alternative hadronic modeling, the data from the X-ray band to the γ -ray band can be well reproduced by proton synchrotron emission, provided they are efficiently accelerated up to energy $2 \times 10^{17} \text{ eV}$ with a power-law index -1.8 . The modeling requires a relatively high jet total luminosity $\sim 10^{49} \text{ erg s}^{-1}$, which exceeds the Eddington luminosity ($\sim 10^{47} \text{ erg s}^{-1}$) for a black hole mass of $8 \times 10^8 M_\odot$ (Nilsson et al. 2009). However, this required luminosity is not a strong argument to disfavour the hadronic origin of 3C 279 emission during the 2015 flare considering that the source was in an exceptionally bright state.

Having estimated the model parameters of each blazar SEDs, the corresponding neutrino flux can be derived. The flux of muon neutrino, $F_{\nu_\mu}(E_{\nu_\mu})$, in all considered scenarios is shown by the light blue line in Figures 1-3. When available, the neutrino flux is compared with the limit imposed by the IceCube detector. This flux can be transformed to the expected observed number of neutrinos in the IceCube detector using its averaged effective area $A_{\text{eff}}(E_\mu)$, which is mostly a function of the incident neutrino energy. For 3HSP J095507.9+355101 and 3C 279, the average area from Aartsen et al. (2019) was considered, while for TXS 0506+056 we used the area released after the observation of IceCube-170922A⁴. The effective area increases with energy and reaches its maximal value for energies above several hundreds of PeV. The expected number of muon neutrinos and anti-neutrinos is computed through

$$N_{\nu_\mu + \bar{\nu}_\mu} = t_{\text{exp}} \int_{E_{\text{min}, \nu_\mu}}^{E_{\text{max}, \nu_\mu}} F_{\nu_\mu}(E_{\nu_\mu}) A_{\text{eff}}(E_{\nu_\mu}) dE_{\nu_\mu} \quad (20)$$

where the minimum and maximum energy of the neutrinos are $E_{\text{min}, \nu_\mu} = 100 \text{ GeV}$ and $E_{\text{max}, \nu_\mu} = 10^9 \text{ GeV}$, respectively, chosen to correspond the limits for the effective area. The expected number of neutrino events depends on the duration of the source activity, t_{exp} , over which the neutrinos are emitted. The neutrino oscillation, within the quasi-two neutrino oscillation assumption, is taken into account by

$$N_{\nu_\mu}^{\text{obs}} = 0.575 N_{\nu_\mu} + 0.425 N_{\nu_e}, \quad (21)$$

where $N_{\nu_\mu}^{\text{obs}}$ is the observable distribution of muon neutrinos, while, N_{ν_μ} and N_{ν_e} are the emitted muon and electron neutrino distributions (Fantini et al. 2018).

The expected number of neutrinos during the 6 months flare of TXS 0506+056 is 0.43 and 0.23 for the hadronic and the lepto-hadronic scenarios, respectively. During the 2014-2015 neutrino flare, our most optimistic model predict 3.0-3.3 neutrinos for a 6 months exposure time (note however that the IceCube observational window was ~ 110 days). However, this lepto-hadronic modeling requires the jet luminosity to reach unrealistic values, $4.9 \times 10^{52} \text{ erg s}^{-1}$, significantly exceeding the Eddington limit. By slightly varying the model parameters, a higher neutrino event count can be estimated, but it always remains below the 13 ± 5 events mark. The neutrino flux directly depends on the proton content in the jet, which is limited by the upper limit of the X-ray luminosity. Our results are in agreement with previous estimations for TXS 0506+056 and confirm that within a one-zone scenarios, 13 ± 5 events from the direction of TXS 0506+056 cannot be explained (Reimer et al. 2019; Rodrigues et al. 2019).

⁴ <https://icecube.wisc.edu/science/data-releases/>

In the case of 3HSP J095507.9+355101, the muon neutrino rate, $N_{\nu_\mu+\bar{\nu}_\mu}/t_{\text{exp}}$, is within $6 \times 10^{-4} - 4.8 \times 10^{-3}$ per day. This implies that under this rate of emission, the expected number of neutrinos to be detected by IceCube in a time corresponding to the duration of the flare is very low. By exploring different parameter sets, [Petropoulou et al. \(2020b\)](#) concluded that in the most promising scenarios, there is a $\sim 1\%$ to $\sim 3\%$ to observe one neutrino over the time characteristic of the long-term emission of 3HSP J095507.9+355101 (years). As the neutrino emission seems to coincide with extreme behaviour of 3HSP J095507.9+355101 in the X-ray band, in principle, a large number of neutrinos could be expected if such an activity continues for a longer period. However, this is not the case for 3HSP J095507.9+355101. Similarly, when considering the flaring activity of 3C 279, a neutrino daily rate as high as 0.15 per day is estimated. However, for a relatively short period of the source activity, from minutes to one day, no neutrino events in the IceCube detector are expected, in agreement with [Abbasi et al. \(2021\)](#).

6 CONCLUSION

Extensive multiwavelength data campaigns from radio to TeV energy bands and simultaneous observations of VHE neutrinos by increasingly more precise experiments pave the way towards a better understanding of highly energetic sources, both in terms of emission mechanism and dynamics. The understanding of the broad SED and neutrino emission requires detailed time-dependent numerical models of the interactions between leptons, photons and hadrons. We have presented a new kinetic model of photo-hadronic and leptonic interactions aiming at studying the emission of optically thin (for Compton scattering) scenarios of relativistic sources (e.g., AGNs and GRBs). Our numerical solution of the kinetic equations for protons, neutrons, pions, muons, neutrinos, pairs, and photons conserves the total energy of the system as well as the number of particles where required. The code takes as an input the spectral injection rate of the particles (e.g., electrons and/or protons), and compute the time evolution of all relevant particles, including the secondaries, as they interact and cool, allowing the computation of the broadband emission spectrum at any given period.

In this paper, we have applied *SOPRANO* to model the SEDs of three blazars, two of which are potentially associated to neutrino emission observed by IceCube. We have assumed different models for the production of the HE component and compute in all cases the expected number of muon neutrinos. The time-dependent nature of the code allowed to follow the evolution of all particles in one dynamical time scale and then assess the proton content in the jet by using the radiative spectrum of either secondaries or initial particles. This is necessary for the estimation of the expected number of neutrinos. Such time-dependent treatment of the particle evolution enabled us to constrain different scenarios of neutrino production by using the limits imposed by the observations in different bands.

7 ACKNOWLEDGEMENTS

NS and SG acknowledge the supported by the Science Committee of RA, in the frames of the research project No 20TTCG-IC015. SG acknowledges the hospitality of the Max Planck Institute for Physics in Munich, where part of this research was completed and the support from German Academic Exchange Service (DAAD) in Armenia via short-term scholarship. DB was supported by the Deutsche Forschungsgemeinschaft (SFB 1258) when most of the

work was done, and presently acknowledges support from the European Research Council via the ERC consolidating grant #773062 (acronym O.M.J.).

DATA AVAILABILITY

The data underlying this article will be shared on reasonable request to the corresponding author.

REFERENCES

- Aartsen M. G., et al., 2013, *Physical Review Letters*, **111**, 021103
 Aartsen M. G., et al., 2019, *European Physical Journal C*, **79**, 234
 Aartsen M. G., et al., 2020, *Phys. Rev. Lett.*, **125**, 121104
 Abbasi R., et al., 2021, *ApJ*, **911**, 67
 Ackermann M., et al., 2016, *ApJ*, **824**, L20
 Ackermann M., et al., 2017, *ApJ*, **837**, L5
 Aleksić J., et al., 2014a, *Science*, **346**, 1080
 Aleksić J., et al., 2014b, *A&A*, **567**, A41
 Ansoldi S., et al., 2018, *ApJ*, **863**, L10
 Araudo A. T., Bosch-Ramon V., Romero G. E., 2013, *MNRAS*, **436**, 3626
 Asano K., Hayashida M., 2015, *ApJ*, **808**, L18
 Asano K., Inoue S., 2007, *ApJ*, **671**, 645
 Atoyan A. M., Dermer C. D., 2003, *ApJ*, **586**, 79
 Beall J. H., Bednarek W., 1999, *ApJ*, **510**, 188
 Begelman M. C., Rudak B., Sikora M., 1990, *ApJ*, **362**, 38
 Belmont R., Malzac J., Marcowith A., 2008, *A&A*, **491**, 617
 Berezhinsky V. S., Gazizov A. Z., 1993, *Phys. Rev. D*, **47**, 4206
 Blandford R., Eichler D., 1987, *Phys. Rep.*, **154**, 1
 Bloom S. D., Marscher A. P., 1996, *ApJ*, **461**, 657
 Blumenthal G. R., 1970, *Phys. Rev. D*, **1**, 1596
 Boettcher M., Schlickeiser R., 1997, *A&A*, **325**, 866
 Bottacini E., Böttcher M., Pian E., Collmar W., 2016, *ApJ*, **832**, 17
 Böttcher M., Baring M. G., 2019, *ApJ*, **887**, 133
 Böttcher M., Reimer A., Sweeney K., Prakash A., 2013a, *ApJ*, **768**, 54
 Böttcher M., Reimer A., Sweeney K., Prakash A., 2013b, *ApJ*, **768**, 54
 Bustamante M., Tamborra I., 2020, arXiv e-prints, [p. arXiv:2009.01306](#)
 Caprioli D., Spitkovsky A., 2014a, *ApJ*, **783**, 91
 Caprioli D., Spitkovsky A., 2014b, *ApJ*, **794**, 46
 Caprioli D., Spitkovsky A., 2014c, *ApJ*, **794**, 47
 Cerruti M., Zech A., Boisson C., Inoue S., 2015a, *MNRAS*, **448**, 910
 Cerruti M., Zech A., Boisson C., Inoue S., 2015b, *MNRAS*, **448**, 910
 Cerruti M., Zech A., Boisson C., Emery G., Inoue S., Lenain J.-P., 2019a, *MNRAS*, **483**, L12
 Cerruti M., Zech A., Boisson C., Emery G., Inoue S., Lenain J. P., 2019b, *MNRAS*, **483**, L12
 Chang J., Cooper G., 1970, *Journal of Computational Physics*, **6**, 1
 Chiaberge M., Ghisellini G., 1999, *MNRAS*, **306**, 551
 Chodorowski M. J., Zdziarski A. A., Sikora M., 1992, *ApJ*, **400**, 181
 Costamante L., et al., 2001, *A&A*, **371**, 512
 Crumley P., Kumar P., 2013, *MNRAS*, **429**, 3238
 Dar A., Laor A., 1997, *ApJ*, **478**, L5
 Dermer C. D., Menon G., 2009, *High Energy Radiation from Black Holes: Gamma Rays, Cosmic Rays, and Neutrinos*
 Diltz C., Böttcher M., Fossati G., 2015, *ApJ*, **802**, 133
 Dimitrakoudis S., Mastichiadis A., Protheroe R. J., Reimer A., 2012, *A&A*, **546**, A120
 Domínguez A., et al., 2011, *MNRAS*, **410**, 2556
 Fantini G., Gallo Rosso A., Vissani F., Zema V., 2018, arXiv e-prints, [p. arXiv:1802.05781](#)
 Finke J. D., Dermer C. D., Böttcher M., 2008, *ApJ*, **686**, 181
 Freedman W. L., et al., 2001, *ApJ*, **553**, 47
 Gao S., Pohl M., Winter W., 2017, *ApJ*, **843**, 109
 Gao S., Fedynitch A., Winter W., Pohl M., 2019a, *Nature Astronomy*, **3**, 88
 Gao S., Fedynitch A., Winter W., Pohl M., 2019b, *Nature Astronomy*, **3**, 88

- Gasparyan S., Sahakyan N., Baghmanyan V., Zargaryan D., 2018, preprint, ([arXiv:1807.02869](https://arxiv.org/abs/1807.02869))
- Ghisellini G., Tavecchio F., 2009, *MNRAS*, **397**, 985
- Ghisellini G., Maraschi L., Treves A., 1985, *A&A*, **146**, 204
- Giannios D., Uzdensky D. A., 2019, *MNRAS*, **484**, 1378
- Giommi P., Padovani P., Oikonomou F., Glauch T., Paiano S., Resconi E., 2020a, *A&A*, **640**, L4
- Giommi P., Glauch T., Resconi E., 2020b, The Astronomer's Telegram, **13394**, 1
- Guo X., Sironi L., Narayan R., 2014, *ApJ*, **794**, 153
- Guo F., et al., 2016, *ApJ*, **818**, L9
- Hümmer S., Rüger M., Spanier F., Winter W., 2010, *ApJ*, **721**, 630
- IceCube Collaboration 2013, *Science*, **342**, 1242856
- IceCube Collaboration 2020, GRB Coordinates Network, **26655**, 1
- IceCube Collaboration et al., 2018a, *Science*, **361**, eaat1378
- IceCube Collaboration et al., 2018b, *Science*, **361**, 147
- Jiang Y.-F., Stone J. M., Davis S. W., 2019, *ApJ*, **880**, 67
- Jiménez Fernández B., van Eerten H., 2021, arXiv e-prints, p. [arXiv:2104.08207](https://arxiv.org/abs/2104.08207)
- Jones F. C., 1968, *Physical Review*, **167**, 1159
- Kantzas D., et al., 2020, *MNRAS*,
- Keivani A., et al., 2018a, *ApJ*, **864**, 84
- Keivani A., et al., 2018b, *ApJ*, **864**, 84
- Kelner S., Aharonian F., 2008, *Physical Review D*, **78**, 034013
- Kirk J. G., Guthmann A. W., Gallant Y. A., Achterberg A., 2000, *ApJ*, **542**, 235
- Kusunose M., Takahara F., 2017, *ApJ*, **835**, 20
- Lipari P., Lusignoli M., Meloni D., 2007, *Phys. Rev. D*, **75**, 123005
- Liu R.-Y., Wang K., Xue R., Taylor A. M., Wang X.-Y., Li Z., Yan H., 2019, *Phys. Rev. D*, **99**, 063008
- Mahadevan R., Narayan R., Yi I., 1996, *ApJ*, **465**, 327
- Mannheim K., 1993, *A&A*, **269**, 67
- Mannheim K., Biermann P. L., 1989, *A&A*, **221**, 211
- Maraschi L., Ghisellini G., Celotti A., 1992, *ApJ*, **397**, L5
- Marcowith A., Malzac J., 2003, *A&A*, **409**, 9
- Mastichiadis A., Kirk J. G., 1995, *A&A*, **295**, 613
- Mastichiadis A., Protheroe R. J., Kirk J. G., 2005, *A&A*, **433**, 765
- Motz J., Olsen H. A., Koch H., 1969, *Reviews of Modern Physics*, **41**, 581
- Mücke A., Protheroe R. J., 2001, *Astroparticle Physics*, **15**, 121
- Mücke A., Engel R., Rachen J. P., Protheroe R. J., Stanev T., 2000, *Computer Physics Communications*, **124**, 290
- Mücke A., Protheroe R. J., Engel R., Rachen J. P., Stanev T., 2003, *Astroparticle Physics*, **18**, 593
- Murase K., Oikonomou F., Petropoulou M., 2018, *ApJ*, **865**, 124
- Nalewajko K., Begelman M. C., Sikora M., 2014, *ApJ*, **789**, 161
- Nilsson K., Pursimo T., Villforth C., Lindfors E., Takalo L. O., 2009, *A&A*, **505**, 601
- Padovani P., Resconi E., Giommi P., Arsioli B., Chang Y. L., 2016, *MNRAS*, **457**, 3582
- Padovani P., et al., 2017, *A&ARv*, **25**, 2
- Padovani P., Giommi P., Resconi E., Glauch T., Arsioli B., Sahakyan N., Huber M., 2018, *MNRAS*, **480**, 192
- Padovani P., Oikonomou F., Petropoulou M., Giommi P., Resconi E., 2019, *MNRAS*, **484**, L104
- Paiano S., Falomo R., Padovani P., Giommi P., Gargiulo A., Uslenghi M., Rossi A., Treves A., 2020, *MNRAS*, **495**, L108
- Paliya V. S., 2015, *ApJ*, **808**, L48
- Paliya V. S., Parker M. L., Fabian A. C., Stalin C. S., 2016, *ApJ*, **825**, 74
- Paliya V. S., Böttcher M., Olmo-García A., Domínguez A., Gil de Paz A., Franckowiak A., Garrappa S., Stein R., 2020, *ApJ*, **902**, 29
- Park J., Caprioli D., Spitkovsky A., 2015, *Physical Review Letters*, **114**, 085003
- Pe'er A., Waxman E., 2005, *ApJ*, **628**, 857
- Petropoulou M., Mastichiadis A., 2015, *MNRAS*, **447**, 36
- Petropoulou M., Nalewajko K., Hayashida M., Mastichiadis A., 2017, *MNRAS*, **467**, L16
- Petropoulou M., et al., 2020a, *ApJ*, **891**, 115
- Petropoulou M., Oikonomou F., Mastichiadis A., Murase K., Padovani P., Vasilopoulos G., Giommi P., 2020b, *ApJ*, **899**, 113
- Reimer A., Böttcher M., Buson S., 2019, *ApJ*, **881**, 46
- Reynoso M. M., Medina M. C., Romero G. E., 2011, *A&A*, **531**, A30
- Righi C., Tavecchio F., Pacciani L., 2019, *MNRAS*, **484**, 2067
- Rodrigues X., Gao S., Fedynitch A., Palladino A., Winter W., 2019, *ApJ*, **874**, L29
- Rybicki G. B., Lightman A. P., 1979, *Radiative processes in astrophysics*
- Sahakyan N., 2018, *ApJ*, **866**, 109
- Sahakyan N., Israyelyan D., Harutyunyan G., Khachatryan M., Gasparyan S., 2020, *MNRAS*, **498**, 2594
- Sikora M., Begelman M. C., Rees M. J., 1994, *ApJ*, **421**, 153
- Sikora M., Sol H., Begelman M. C., Madejski G. M., 1996, *MNRAS*, **280**, 781
- Sikora M., Stawarz Ł., Moderski R., Nalewajko K., Madejski G. M., 2009, *ApJ*, **704**, 38
- Summerlin E. J., Baring M. G., 2012, *ApJ*, **745**, 63
- Tavecchio F., Ghisellini G., 2008, *MNRAS*, **385**, L98
- Tavecchio F., Ghisellini G., 2016, *MNRAS*, **456**, 2374
- Urry C. M., Padovani P., 1995, *PASP*, **107**, 803
- Vurm I., Poutanen J., 2009, *ApJ*, **698**, 293
- Xue R., Liu R.-Y., Wang X.-Y., Yan H., Böttcher M., 2019a, *ApJ*, **871**, 81
- Xue R., Liu R.-Y., Petropoulou M., Oikonomou F., Wang Z.-R., Wang K., Wang X.-Y., 2019b, *ApJ*, **886**, 23
- Zatsepin G., Kuz'min V., 1962, *Soviet Physics JETP*, **14**
- Zech A., Cerruti M., Mazin D., 2017, *A&A*, **602**, A25
- Zyla P. A., et al., 2020, *Progress of Theoretical and Experimental Physics*, **2020**
- de Jager O. C., Harding A. K., Michelson P. F., Nel H. I., Nolan P. L., Sreekumar P., Thompson D. J., 1996, *ApJ*, **457**, 253

APPENDIX A: PHYSICAL PROCESSES IN SOPRANO AND THEIR KINETIC EQUATIONS

In the current version of *SOPRANO*, the isotropic kinetic equations for photons, electrons and positrons (considered as one species, see below), protons, neutrons, charged and neutral pions, muons, neutrino and anti-neutrino of all relevant⁵ flavors are evolved in time. For the photon distribution function, we assign n_{ph} to be the number of photons per unit volume per hertz. We further define N_i to be the number of particles of i species per unit volume per unit Lorentz factor of particle i . Here, i can be all leptons and all hadrons. Finally, we define N_{ν_i} as the number of neutrinos of i flavour per unit volume per GeV. In our numerical approach, all hadrons and leptons are considered relativistic with $\gamma_i \geq 1$. This appendix gives an overview of the kinetic equations, of the cross-sections and of the kinetic equations used in *SOPRANO* for all considered interactions. In Appendix B, we detail the numerical prescription.

A1 Kinetic equations for all particles

Here, we summarize all terms appearing in the kinetic equations for all particle species. We denote Q , S and C as the source, sink and cooling terms, respectively. The contribution of inverse Compton scattering is denoted by R_{IC} for the photons and it is a cooling term for the leptons. Detailed expressions for the interaction kernels are given in the next subsections of this appendix.

- *Photons* are produced by the synchrotron radiation of all charged particles and by the decay of neutral pions, π_0 . They are absorbed by pair production and redistributed in energy by inverse Compton scattering. We neglect the absorption of photons in the photo-pion and photo-pair processes. We did not consider synchrotron self-absorption and are planning to include it in the next version. The resulting kinetic equation takes the form

$$\frac{\partial n_{\text{ph}}}{\partial t} = -S_{\gamma\gamma \rightarrow e^+e^-} + Q_{\pi_0} + R_{\text{IC}} + \sum_{i \in [p, \mu^\pm, \pi^\pm, e^\pm]} Q_{\text{synch}}^i, \quad (\text{A1.1})$$

where the last sum runs on all charged particles.

- *Leptons* (electrons and positrons) are considered as a single species. They are created by muon decay, Bethe-Heitler photo-pair production and two photons recombination. They also undergo synchrotron cooling such that the final kinetic equation reads as

$$\frac{\partial N_{e^\pm}}{\partial t} = Q_{\mu^\pm} + Q_{p\gamma \rightarrow e^+e^-} + Q_{\gamma\gamma \rightarrow e^+e^-} + C_{\text{IC}} + C_{\text{synch}}. \quad (\text{A1.2})$$

- *Protons* are losing energy by synchrotron emission, photo-pair and photo-pion interactions. Protons are produced through photo-hadronic interactions between photons and neutrons, and are turned to neutrons for a substantial fraction of photo-pion interactions. The kinetic equation takes the form

$$\frac{\partial N_p}{\partial t} = C_{p\gamma \rightarrow p\pi} + C_{p\gamma \rightarrow e^+e^-} + C_{\text{synch}} - S_{\gamma p \rightarrow n\pi} + Q_{\gamma n \rightarrow p\pi}. \quad (\text{A1.3})$$

- *Neutrons* are produced in photo-pion interactions and turned to protons by the same process. The kinetic equation takes the form

$$\frac{\partial N_n}{\partial t} = -S_{n\gamma \rightarrow p\pi} + Q_{p\gamma \rightarrow n\pi} + C_{n\gamma \rightarrow n\pi}. \quad (\text{A1.4})$$

In the current version of the code, we do not include neutron decay. Indeed, for the very large particle Lorentz factor involved, neutrons would escape the source before decaying. In principle, neutrinos produced by neutron decay should contribute to the observed overall signal. But since we are considering models in which the neutron number is always much smaller than the proton number, we can safely neglect this contribution. Note that numerically investigating a model similar to that of [Atoyan & Dermer \(2003\)](#) would require a proper treatment of neutron decay.

- *Charged pions*, π_+ and π_- , are produced by photo-pion interactions. Then, they cool via synchrotron emission and decay. The kinetic equation for both species takes the form

$$\frac{\partial N_{\pi_\pm}}{\partial t} = Q_{p\gamma \rightarrow \pi} + Q_{n\gamma \rightarrow \pi} - S_{\pi} + C_{\text{synch}}. \quad (\text{A1.5})$$

The kinetic equations were solved independently for π^+ and π^- since the branching ratio in photo-pion production is different for negative and positive pions. This impacts the production ratio between the different neutrino species further.

- *Neutral pions* have a kinetic equation similar to that of charged pions but without synchrotron cooling.
- *Muons* are produced from the decay of charged pions. They lose energy by synchrotron radiation and decay. Therefore, the kinetic equation is

$$\frac{\partial N_{\mu_\pm}}{\partial t} = Q_{\pi_\pm} - S_{\mu_\pm} + C_{\text{synch}}. \quad (\text{A1.6})$$

- *Muon and electron neutrinos and anti-neutrinos* are produced in the decay of pions and muons. We consider the two flavours independently, but neutrino and anti-neutrinos of the same flavour are combined.

$$\frac{\partial N_{\nu}}{\partial t} = Q_{\pi_\pm} + Q_{\mu_\pm}. \quad (\text{A1.7})$$

For each of the processes, the details of the terms Q , S , C and R are given in the next subsections of Appendix A together with the cross-sections used in *SOPRANO*.

⁵ τ neutrino cannot be produced by photo-hadronic interactions.

A2 Synchrotron emission and cooling

In *SOPRANO*, all charged particles lose their energy by synchrotron radiation as soon as a magnetic field is specified. Our current treatment does not include synchrotron self-absorption, which will be added in a future update. For each charged particles, we describe the evolution of the distribution function due to synchrotron losses by a diffusion equation in energy space

$$\frac{\partial N_i}{\partial t} = \frac{1}{m_i c^2} \frac{\partial}{\partial \gamma_i} \left(N_i \int_0^\infty j_{\text{synch}}(\nu, \gamma_i) d\nu \right), \quad (\text{A2.1})$$

while the photon kinetic equation is given by an integro-differential type equation:

$$\frac{\partial n_{\text{ph}}}{\partial t} = \int_1^\infty N_i(\gamma_i) \frac{j_{\text{synch}}}{h\nu}(\nu, \gamma_i) d\gamma_i. \quad (\text{A2.2})$$

The synchrotron emissivity j_{synch} is given in the relativistic approximation by

$$j_{\text{synch}}(\nu) = \frac{\sqrt{3} q^3 B}{m_i c^2} \int_0^{\pi/2} \sin(\theta_p) F(X) d\theta_p \quad (\text{A2.3})$$

with $X = \nu/\nu_c$,

$$\nu_c = \frac{3}{4\pi} \gamma_i^2 \frac{qB}{m_i c} \sin(\theta_p), \quad (\text{A2.4})$$

and

$$F(X) = X \int_X^\infty K_{5/3}(\xi) d\xi \quad (\text{A2.5})$$

with $K_{5/3}$ the modified Bessel function. This expression fails when the particle Lorentz factor tends towards one, in which case expression suitable with cyclo-synchrotron should be used (Mahadevan et al. 1996; Marcowith & Malzac 2003). Therefore, in our numerical models, synchrotron emission due to mildly-relativistic particles is inaccurate. In practice, this parameter space is not relevant for blazars or for optically thin emission models of GRBs.

A3 Inverse Compton scattering.

For the rate of Compton scattering of an electron with Lorentz factor γ interacting with an isotropic distribution of photons of energy $x_1 = h\nu_1/(m_e c^2)$, we consider the relativistic approximation given by Jones (1968)

$$R(\gamma, x_1 \rightarrow x_2) \equiv \frac{dN}{dt dx_2} = \frac{3c}{4} \frac{\sigma_T}{x_1 \gamma^2} \left[2q \ln(q) + (1+2q)(1-q) + \frac{1}{2} \frac{(4x_1 \gamma q)^2}{1+4x_1 \gamma q} (1-q) \right], \quad (\text{A3.1})$$

where $x_2 = h\nu_2/(m_e c^2)$ is the energy of the scattered photons, and

$$q = \frac{x_2}{4x_1 \gamma^2 \left(1 - \frac{x_2}{\gamma} \right)}, \quad (\text{A3.2})$$

is limited to $q < 1$ and $q > 1/(4\gamma^2)$. This approximation to the exact cross-section is often used for blazar modeling. It is accurate for large electron Lorentz factors, relevant for those objects. This approximation also implies that electrons can only lose energy and photons can only gain energy. Therefore, it is not suitable to describe the heating of electrons by the photon field.

For the relativistic electrons considered in *SOPRANO*, the kinetic equation takes the form of a diffusion equation

$$\frac{\partial}{\partial t} (N_{e^\pm}) = \frac{1}{m_e c^2} \frac{\partial}{\partial \gamma_e} (P_c N_{e^\pm}), \quad (\text{A3.3})$$

where the power radiated by Compton scattering is

$$P_c(\gamma) = m_e c^2 \int_{x_1}^\infty \int_{x_2}^\infty dx_1 dx_2 R(\gamma, x_1 \rightarrow x_2) n_{\text{ph}}(x_1) (x_2 - x_1). \quad (\text{A3.4})$$

On the other hand, we preserve the full integro-differential expression for the photon kinetic equations since for each inverse Compton scattering off relativistic electrons, photons gain a large amount of energy compared to their initial energy :

$$\frac{\partial n_{\text{ph}}}{\partial t}(x_2) = \int_\gamma^\infty \int_{x_1}^\infty d\gamma dx_1 R(\gamma, x_1 \rightarrow x_2) N_{e^\pm}(\gamma) n_{\text{ph}}(x_1) - n_{\text{ph}}(x_2) \int_\gamma^\infty \int_{x_1}^\infty d\gamma dx_1 R(\gamma, x_2 \rightarrow x_1) N_{e^\pm}(\gamma). \quad (\text{A3.5})$$

The first term represent the redistribution of photons of energy x_1 to x_2 and the second term represent the redistribution of photons of energy x_2 to all other possible energies.

A4 Pair production

For the pairs, the kinetic equation of the photon-photon annihilation process reads

$$\frac{\partial N_e}{\partial t} = c \int_{x_1} \int_{x_2} n_{\text{ph}}(x_1) n_{\text{ph}}(x_2) \sigma_{2\gamma \rightarrow e^\pm}(x_1, x_2 \rightarrow \gamma) dx_1 dx_2. \quad (\text{A4.1})$$

For the photons, the kinetic equation can be written

$$\frac{\partial n_{\text{ph}}}{\partial t}(x_1) = -n_\gamma(x_1) \int_{x_2} n_{\text{ph}}(x_2) \sigma_{2\gamma \rightarrow e^\pm}^0(x_1, x_2) dx_2, \quad (\text{A4.2})$$

where

$$\sigma_{2\gamma \rightarrow e^\pm}^0 = 2 \int_{\gamma} \sigma_{2\gamma \rightarrow e^\pm}(x_1, x_2, \gamma) d\gamma. \quad (\text{A4.3})$$

For the cross-section, we use the formula given by [Boettcher & Schlickeiser \(1997\)](#). It is recall here for convenience

$$\sigma_{2\gamma \rightarrow e^\pm}(x_1, x_2 \rightarrow \gamma) = \frac{3}{4} \frac{\sigma_T c}{x_1^2 x_2^2} \left(\frac{\sqrt{E^2 - 4\alpha_{\text{cm}}^2}}{4} + H_+ + H_- \right) \bigg|_{\alpha_{\text{cm}}^L}^{\alpha_{\text{cm}}^U}, \quad (\text{A4.4})$$

where the center of mass energy α_{cm} is given by

$$\alpha_{\text{cm}} = \sqrt{\frac{x_1 x_2}{2}}, \quad (\text{A4.5})$$

and

$$\begin{cases} E = x_1 + x_2 \\ c_\pm = (x_{1,2} - \gamma)^2 - 1 \\ d_\pm = x_{1,2}^2 + x_1 x_2 \pm \gamma(x_2 - x_1) \\ \alpha_{\text{cm}}^{a,b} = \sqrt{1/2} \sqrt{\gamma(E - \gamma) + 1 \pm \sqrt{[\gamma(E - \gamma) + 1]^2 - E^2}} \\ \alpha_{\text{cm}}^U = \min(\sqrt{x_1 x_2}, \alpha_{\text{cm}}^a) \\ \alpha_{\text{cm}}^L = \max(1, \alpha_{\text{cm}}^b) \end{cases} \quad (\text{A4.6})$$

Finally for $c \neq 0$, the H functions are defined by

$$H_\pm = - \frac{\alpha_{\text{cm}}}{8\sqrt{x_1 x_2 + c_\pm \alpha_{\text{cm}}^2}} \left(\frac{d_\pm}{x_1 x_2} + \frac{2}{c_\pm} \right) + \frac{1}{4} \left(2 - \frac{x_1 x_2 - 1}{c_\pm} \right) I_\pm + \frac{\sqrt{x_1 x_2 + c_\pm \alpha_{\text{cm}}^2}}{4} \left(\frac{\alpha_{\text{cm}}}{c_\pm} + \frac{1}{\alpha_{\text{cm}} x_1 x_2} \right), \quad (\text{A4.7})$$

where

$$I_\pm = \begin{cases} \frac{1}{\sqrt{c_\pm}} \ln \left(\alpha_{\text{cm}} \sqrt{c_\pm} + \sqrt{x_1 x_2 + c_\pm \alpha_{\text{cm}}^2} \right) & c_\pm > 0, \\ \frac{1}{\sqrt{c_\pm}} \arcsin \left(\alpha_{\text{cm}} \sqrt{-\frac{c_\pm}{x_1 x_2}} \right) & c_\pm < 0, \end{cases} \quad (\text{A4.8})$$

while for $c_\pm = 0$, we have

$$H_\pm = \left(\frac{\alpha_{\text{cm}}^3}{12} - \frac{\alpha_{\text{cm}} d_\pm}{8} \right) \frac{1}{(x_1 x_2)^{3/2}} + \left(\frac{\alpha_{\text{cm}}^2}{6} + \frac{\alpha_{\text{cm}}}{2} + \frac{1}{4\alpha_{\text{cm}}} \right) \frac{1}{\sqrt{x_1 x_2}}. \quad (\text{A4.9})$$

A5 Bethe-Heitler pair production

Photo-pair production, also called Bethe-Heitler process, is the creation of an electron positron pair by the interaction between a proton and a photon. The cross section of this process is given by the formula 3D-2000 of [Motz et al. \(1969\)](#), see also [Blumenthal \(1970\)](#) and [Kelner & Aharonian \(2008\)](#), which we recall here for convenience:

$$\begin{aligned} \frac{d^2 \sigma}{dE_- d\mu} = & \left(\frac{\alpha Z^2 r_0^2 p_- p_+}{2k^3} \right) \left[-4 \sin^2(\theta) \frac{2E_-^2 + 1}{p_-^2 \Delta_-^4} + \frac{5E_-^2 - 2E_+ E_- + 3}{p_-^2 \Delta_-^2} + \frac{p_-^2 - k^2}{T^2 \Delta_-^2} + \frac{2E_+}{p_-^2 \Delta_-} \right. \\ & + \frac{Y}{p_- p_+} \left(2E_- \sin^2(\theta) \frac{3k + p_-^2 E_+}{\Delta_-^4} + \frac{2E_-^2 (E_-^2 + E_+^2) - (7E_-^2 + 3E_+ E_- + E_+^2) + 1}{\Delta_-^2} + \frac{k(E_-^2 - E_- E_+ - 1)}{\Delta_-} \right) \\ & \left. - \frac{\delta_+}{p_+ T} \left(\frac{2}{\Delta_-^2} - \frac{3k}{\Delta_-} - \frac{k(p_-^2 - k^2)}{T^2 \Delta_-} \right) - \frac{2y_+}{\Delta_-} \right], \end{aligned} \quad (\text{A5.1})$$

where

$$E_+ = k - E_- \quad p_+ = \sqrt{p_+^2 - 1} \quad p_- = \sqrt{E_-^2 - 1} \quad (\text{A5.2})$$

$$T = \sqrt{k^2 + p_-^2 - 2kp_- \cos(\theta)} \quad Y = \frac{2}{p_-^2} \ln \left(\frac{E_+ E_- + p_+ p_- + 1}{k} \right) \quad (\text{A5.3})$$

$$y_+ = \frac{1}{p_+} \ln \left(\frac{E_+ + p_+}{E_+ - p_+} \right) \quad \delta_+ = \ln \left(\frac{T + p_+}{T - p_+} \right). \quad (\text{A5.4})$$

The kinetic equation for the production of pairs is given by

$$\frac{\partial}{\partial t} (N_{e^\pm}(\gamma_e)) = c \int_{\gamma_p m_p > \gamma_e m_e} dE_p N_p \frac{dN_e}{dE_e}. \quad (\text{A5.5})$$

The pair spectrum is given by [Kelner & Aharonian \(2008\)](#)

$$\frac{dN_e^-}{dE_e} = \frac{1}{2\gamma_p^3} \int_{x=\frac{(\gamma_p+E_e)^2}{4\gamma_p^2 E_e}}^{\infty} \int_{\omega=\frac{(\gamma_p+E_e)^2}{2\gamma_p E_e}}^{2\gamma_p x} \times \int_{E_-=\frac{\gamma_p^2+E_e^2}{2\gamma_p E_e}}^{\omega-1} \frac{dE_- d\omega dx}{p_-} \frac{n_{\text{ph}}(x)}{x^2} W(\omega, E_-, \xi), \quad (\text{A5.6})$$

where ϵ is the photon energy in unit of electron rest mass energy. The kinetic equation for the protons is obtained from consideration of energy conservation

$$\frac{\partial N_p(\gamma_p)}{\partial t} = \frac{\partial (P_{\text{BH}} N_p)}{\partial \gamma_p} \quad (\text{A5.7})$$

where the power emitted by Bethe-Heitler is given by

$$P_{\text{BH}} = \int \gamma_e m_e c^2 \frac{dN_{e^\pm}}{dt} \quad (\text{A5.8})$$

A6 Photo-hadronic interaction : pion production

Photo-pion production is the interaction between a proton and a photon mostly producing pions. This interaction can be divided into four channels : resonance, direct production, multi-production and fragmentation. In the following, we neglect the contribution from fragmentation and plan its inclusion for future studies. For the sake of presentation, in this subsection only, we change the energy unit of the photon distribution from frequency ν to energy ϵ in GeV. Following [Hümmer et al. \(2010\)](#), the spectral production rate of each pion species (π^+ , π^- and π^0) can be written as

$$\frac{dN_\pi}{dt} = \sum_{IT} M_{IT} \int_{\gamma_p} \int_{\epsilon} d\gamma_p d\epsilon N_p n_{\text{ph}} R_{IT}(\gamma_p, \nu \rightarrow \gamma_\pi), \quad (\text{A6.1})$$

where the index IT spans all resonances, the two direct production channels, and multi production channels. In this equation M^{IT} is the multiplicity of each interaction. This coefficient takes a different value for each interaction and each pion species. Finally, the rate of interaction is given by [Kelner & Aharonian \(2008\)](#)

$$R_{IT} = \frac{c}{2\gamma_p^2 \beta_p \epsilon^2} \int_{\epsilon_{\text{th}}}^{2\gamma_p \epsilon} d\epsilon_r \epsilon_r \int_{\psi} d\psi \frac{\partial \sigma_{p\gamma}(\epsilon_r, \psi)}{\partial \psi} \delta(E_\pi - \xi), \quad (\text{A6.2})$$

where the threshold energy ϵ_{th} is constrained by the kinematics of the reaction, ϵ_r is the energy of the photon in the frame comoving with the proton, ψ is the cosine of the comoving (in the proton rest-frame) angle between the photon direction and the axis representing the direction of the proton in the lab frame, the differential represent the angular distribution of the reaction and ξ is the pion energy obtained from the kinematics. For a detailed discussion, on the kinematics, see [Begelman et al. \(1990\)](#); [Berezinsky & Gazizov \(1993\)](#) and [Hümmer et al. \(2010\)](#).

A6.1 Photo-pion production : resonances

For the cross-section of the nine resonances considered in this work, we consider the Breit-Wigner approximation

$$\sigma^{IT}(\epsilon_r) = B^{IT} \frac{s}{\epsilon_r^2} \frac{\sigma_0^{IT} (\Gamma^{IT})^2 s}{(s - (M^{IT})^2)^2 + (\Gamma^{IT})^2 s}, \quad (\text{A6.3})$$

where $s = m_p^2 + 2m_p \epsilon_r$ is the total energy in the center of mass. The parameters σ^{IT} , B^{IT} , Γ^{IT} and M^{IT} are given by [Mücke et al. \(2000\)](#); [Hümmer et al. \(2010\)](#) and in the review of Particle Data Group ([Zyla et al. 2020](#)). The nine resonances used are the ones of [Mücke et al. \(2000\)](#). Contrary to the simple model used by [Hümmer et al. \(2010\)](#), we include the angular dependence of the Δ meson decay for R_1 type resonances, as given by table 3 of [Mücke et al. \(2000\)](#).

A6.2 Photo-pion production : direct production

For the direct production, we use the parametric cross-sections given by [Mücke et al. \(2000\)](#)

$$\sigma_{N\pi}(\epsilon_r) = 92.7\mathfrak{P}(\epsilon_r, 0.152, 0.25, 2) + 40 \exp\left(-\frac{(\epsilon_r - 0.29)^2}{0.002}\right) - 15 \exp\left(-\frac{(\epsilon_r - 0.37^2)}{0.002}\right), \quad (\text{A6.4})$$

$$\sigma_{\Delta\pi}(\epsilon_r) = 37.7\mathfrak{P}(\epsilon_r, 0.4, 0.6, 2), \quad (\text{A6.5})$$

where the function \mathfrak{P} is 0 if $\epsilon_r \leq \epsilon_{\text{th}}$ and

$$\mathfrak{P}(\epsilon_r, \epsilon_{\text{th}}, \epsilon_{\text{max}}, \alpha) = \left(\frac{\epsilon_r - \epsilon_{\text{th}}}{\epsilon_{\text{max}} - \epsilon_{\text{th}}}\right)^{A-\alpha} \left(\frac{\epsilon_r}{\epsilon_{\text{max}}}\right)^{-A} \quad (\text{A6.6})$$

otherwise. Here, $A = \alpha\epsilon_{\text{max}}/\epsilon_{\text{th}}$. We also include the angular dependence coming from the distribution of the t -Mandelstam variable as explained in [Mücke et al. \(2000\)](#).

A6.3 Photo-pion production : multi-pion production

For the multi-production channel, it is not possible to resort to simple integral expressions. Therefore, we use the approximation developed by [Hümmer et al. \(2010\)](#). It provides a simple and convenient form for the pion spectrum, while the multiplicities are approximated from results of Sophia ([Mücke et al. 2000](#)).

For completeness, we give here the expressions of the pion spectrum:

$$\frac{\partial N_\pi}{\partial E_\pi} = \frac{cm_p}{E_\pi} \sum_{IT} N_p \left(\frac{E_\pi}{\xi^{IT}}\right) \int_{\epsilon_{\text{th}}}^{\infty} dy n_\gamma \left(\frac{m_p y \xi^{IT}}{E_\pi}\right) M^{IT} f^{IT}(y), \quad (\text{A6.7})$$

where

$$f^{IT} = \begin{cases} 0 & 2y < \epsilon_{\text{min}}^{IT} \\ \frac{\sigma^{IT}}{(4y^2)} (4y^2 - \epsilon_{\text{min}}^{IT^2}) & \epsilon_{\text{min}}^{IT} \leq 2y < \epsilon_{\text{max}}^{IT} \\ \frac{\sigma^{IT}}{(4y^2)} (\epsilon_{\text{max}}^{IT^2} - \epsilon_{\text{min}}^{IT^2}) & \epsilon_{\text{max}}^{IT} \leq 2y. \end{cases} \quad (\text{A6.8})$$

The parameters for the 14 interactions making the approximation are given in Table 6 of [Hümmer et al. \(2010\)](#).

A7 Particle decay

We consider the decay of charged pions

$$\begin{cases} \pi^+ \rightarrow \mu^+ + \nu_\mu, \\ \pi^- \rightarrow \mu^- + \bar{\nu}_\mu, \end{cases} \quad (\text{A7.1})$$

of neutral pions

$$\pi^0 \rightarrow 2\gamma, \quad (\text{A7.2})$$

and of muons

$$\begin{cases} \mu^- \rightarrow e^- + \nu_e + \bar{\nu}_\mu, \\ \mu^+ \rightarrow e^+ + \bar{\nu}_e + \nu_\mu. \end{cases} \quad (\text{A7.3})$$

The kinetic equation of the decaying particle is given by

$$\frac{\partial N_i}{\partial t} = -\frac{N_i}{\tau_i \gamma_i} \quad (\text{A7.4})$$

where τ_i is the mean-life time of the particle which decays, and γ_i its Lorentz factor. The kinetic equation for the daughter particle is given by

$$\frac{\partial N_j}{\partial t}(E_j) = \int_{E_i > E_j}^{\infty} \frac{N_i}{\tau_i \gamma_i} F(E_i, E_j) dE_i, \quad (\text{A7.5})$$

where $F(E_i, E_j)$ is the spectrum of particle j at energy E_j produced by a parent particle of energy E_i .

The neutrino spectrum from charged pion decay is given by [Lipari et al. \(2007\)](#)

$$F(E_\pi, E_\nu) = \frac{1}{E_\pi} \frac{1}{1 - r_\pi} H\left(1 - r_\pi - \frac{E_\nu}{E_\pi}\right), \quad (\text{A7.6})$$

where $r_\pi = (m_\mu/m_\pi)^2$.

The photon spectrum obtained from neutral pion decay is given by

$$F(E_{\pi_0}, E_\gamma) = \frac{2}{E_{\pi_0}}, \quad (\text{A7.7})$$

where the factor 2 comes from the fact that two photons are created in the decay.

For the electron and neutrino spectra, we do not use the expression given by [Zatsepin & Kuz'min \(1962\)](#), but resort to the simpler relativistic approximation of [Lipari et al. \(2007\)](#)

$$F_{\nu_e}(E_{\nu_e}, E_\mu) = \frac{2 - 6x^2 + 4x^3}{E_\mu}, \quad (\text{A7.8})$$

$$F_{\nu_\mu}(E_{\nu_\mu}, E_\mu) = F_e(E_e, E_\mu) = \frac{\frac{5}{3} - 3x^2 + \frac{4}{3}x^3}{E_\mu}, \quad (\text{A7.9})$$

where $x = E_i/E_\mu$ for each particle species i .

A8 Photon and particle escape

When dealing with a one-zone model, since the emitting region is assumed to be shaped like a blob, all effects due to photon transport are neglected. Moreover, since we are considering optically thin plasma, photons cannot accumulate in the emission region for an arbitrarily large amount of time. Indeed, they would escape the region in which they are produced in a time of the order of the crossing time

$$t_{\text{ph}}^{\text{esc}} \sim \frac{2R}{3c}, \quad (\text{A8.1})$$

where R is the comoving size. In principle, charged particles could remain longer inside the emitting region. Therefore, particle escape can be treated by adding a term to the kinetic equation of the form

$$\frac{\partial N_i}{\partial t} = \frac{N_i}{\mathfrak{T}_i t_{\text{ph}}^{\text{esc}}}, \quad (\text{A8.2})$$

$$\frac{\partial n_{\text{ph}}}{\partial t} = \frac{n_\gamma}{t_{\text{ph}}^{\text{esc}}}, \quad (\text{A8.3})$$

where $\mathfrak{T}_i = t_i^{\text{esc}}/t_{\text{ph}}^{\text{esc}}$ is a parameter that is specified for each runs. It represents the time increase it takes for a particle to escape the system as compared to a photon. In other words, particle escape is used to crudely represent the finiteness of the emitting region. In this work, we did not consider particle escape. Instead, we evolve the distributions until a comoving time equal to the dynamical time scale.

APPENDIX B: NUMERICAL DISCRETIZATION AND PRESCRIPTION IN *SOPRANO*

In order to numerically integrate the kinetic equations presented in Section A, a numerical grid for the energy of all particles is introduced. In this work, *SOPRANO* uses a grid of bins equally space in logarithmic of the energy⁶. Table B1 gives the grid characteristics for each types of particle, that is to say the number of energy bins, together with the minimum and maximum energies. For the energy discretization, we use the approach of the discontinuous Galerkin method, that we restrain to first order for this paper⁷. On each energy cell I , we approximate the distribution function by a polynomial, while we use for basis the Legendre polynomial basis. Therefore, on each energy cell I , the distribution function is approximated by

$$N_i^I(t, x) = N_{i,0}^I(t) L_0^I(x) \quad (\text{B.1})$$

where the first order Legendre polynomial on the energy cell I is

$$L_0^I = \frac{1}{\sqrt{x_{I+1/2} - x_{I-1/2}}} \equiv \frac{1}{\sqrt{||I||}} \quad (\text{B.2})$$

Here $x_{I\pm(1/2)}$ are the energy boundaries of cell I and where we introduced the additional notation $||I|| = (x_{I+1/2} - x_{I-1/2})$. In the following we will use interchangeably $N_i^I \equiv N_{i,0}^I$.

We seek the weak formulation of all kinetic equations presented in Appendix A on each energy interval I . For this, we multiply both sides of any of the kinetic equation by L_0 and integrate over I . After simplification, we obtain a system of differential equations for all $N_{i,0}^I$. This specific discretization and the structure of the kinetic equation allows us to retrieve a numerical method which conserves energy and the number of particles when they are conserved. Time discretization is achieved via implicit first order Euler method. leptonic processes, which involved terms of the form $n_i n_j$. Below, we give details on the numerical discretisation on a couple of example and give additional details for specific processes when needed.

⁶ Note that our numerical method does not require a uniform grid. Since, it is based on finite volume, we can refine the grid in one or several energy bands of interest (static mesh refinement). In this way, we can provide more detailed results in those specific bands, while the rest of the domain is coarse for faster numerical estimation. This numerical technique will be used in future works, in which we will study the shape of the spectral peaks.

⁷ We have implemented some of the processes with reconstruction up to order 2, but this numerical technique is not included in the current paper

Particle	Number of energy cells	Minimum of the grid	Maximum of the grid
Photons :	150	$\nu = 10^{-2} \text{ Hz}$	$\nu = 10^{30} \text{ Hz}$
Leptons :	130	$\gamma_{e^\pm} = 1.2$	$\gamma_{e^\pm} \times 10^{13}$
Hadrons :	100	$\gamma_h = 1.2$	$\gamma_h = 10^{11}$
Neutrinos :	100	$E_\nu = 10^{-3} \text{ GeV}$	$E_\nu = 10^{11} \text{ GeV}$

Table B1. Characteristics of the numerical grids used by *SOPRANO* for the numerical models of this work. The cells are equally space in logarithmic scale.

For the sake of the example, consider the synchrotron process and its associated kinetic equations. Without synchrotron self-absorption, the treatment of synchrotron losses and photon production is heavily simplified. We start by the photon given by Equation A2.1. Multiplying both side by L_0^J and integrating gives

$$\frac{\partial n_{\text{ph}}^I}{\partial t} = \frac{1}{h\sqrt{||J||}} \sum_K \frac{N_i^K}{\sqrt{||K||}} \int_K \int_I \frac{j_{\text{synch}}^i(\nu, \gamma_i)}{\nu} d\nu d\gamma_i, \quad (\text{B.3})$$

where N_i represent any charged particle. We follow the same procedure for the charge particle equation and after an integration by part, the kinetic equation can be put into the form

$$\frac{\partial N_i^K}{\partial t} = \int_K L_0^K \frac{\partial}{\partial \gamma_k} [P_{\text{synch}} N_i^K L_0^K] d\gamma_i = \int \frac{\partial L_0^K}{\partial \gamma_i} [P_{\text{synch}} N_i^K L_0^K] d\gamma_i - \frac{1}{\sqrt{K}} [F_{K+\frac{1}{2}} - F_{K-\frac{1}{2}}]. \quad (\text{B.4})$$

In this last expression, only the second term is non-null. In order to obtain an expression for the numerical fluxes $F_{K+1/2}$ on the right-hand side, we consider the energy lost by particles and that gain by the photons. The total energy gain by the photons is

$$\frac{\partial E_{\text{ph}}}{\partial t} = \frac{\partial}{\partial t} \left(\sum_J \int_J n_{\text{ph}}^J L_0^J h\nu d\nu \right) = \sum_J \frac{\nu_{J+\frac{1}{2}} - \nu_{J-\frac{1}{2}}}{2||J||} \sum_K \frac{N_i^K}{\sqrt{||K||}} \int_K \int_J \frac{j_{\text{synch}}^i(\nu, \gamma_i)}{\nu} d\gamma_i d\nu, \quad (\text{B.5})$$

where the last equality is obtained after using Equation B.3. Turning to the energy lost by the charged particles, we have

$$\frac{\partial E_i}{\partial t} = m_i c^2 \sum_K \frac{\partial N_i^K}{\partial t} \frac{\gamma_{i,K+\frac{1}{2}}^2 - \gamma_{i,K-\frac{1}{2}}^2}{2\sqrt{||K||}}. \quad (\text{B.6})$$

Inserting the expression for the time derivative of the distribution function coefficients, and reorganising the summation it comes

$$\frac{\partial E_i}{\partial t} = m_i c^2 \left[-\frac{\gamma_{i,\frac{1}{2}}^2 - \gamma_{i,-\frac{1}{2}}^2}{2(\gamma_{i,\frac{1}{2}} - \gamma_{i,-\frac{1}{2}})} F_{-\frac{1}{2}} + \frac{\gamma_{i,\xi+\frac{1}{2}}^2 - \gamma_{i,\xi-\frac{1}{2}}^2}{2(\gamma_{i,\xi+\frac{1}{2}} - \gamma_{i,\xi-\frac{1}{2}})} F_{\xi+\frac{1}{2}} + \sum_K \left(\frac{\gamma_{i,K+\frac{1}{2}}^2 - \gamma_{i,K-\frac{1}{2}}^2}{(\gamma_{i,K+\frac{1}{2}} - \gamma_{i,K-\frac{1}{2}})} - \frac{\gamma_{i,K+\frac{3}{2}}^2 - \gamma_{i,K+\frac{1}{2}}^2}{(\gamma_{i,K+\frac{3}{2}} - \gamma_{i,K+\frac{1}{2}})} \right) \frac{F_{K+\frac{1}{2}}}{2} \right] \quad (\text{B.7})$$

where in this specific equation ξ represent the number of cells of the grid for particle species i . We assume that no particle diffuse out of the energy grid. This gives $F_\xi = F_{-\frac{1}{2}} = 0$. Inverting the summation order in Equation B.5, and identifying the term gives the expression of the fluxes

$$\mathcal{F}_{K+\frac{1}{2}} = \frac{1}{m_i c^2} \frac{N_{i,0}^{K+1} / \sqrt{\gamma_{i,K+\frac{3}{2}} - \gamma_{i,K+\frac{1}{2}}}}{\left[\frac{\gamma_{i,K+\frac{1}{2}}^2 - \gamma_{i,K-\frac{1}{2}}^2}{\gamma_{i,K+\frac{1}{2}} - \gamma_{i,K-\frac{1}{2}}} \right] - \left[\frac{\gamma_{i,K+\frac{3}{2}}^2 - \gamma_{i,K+\frac{1}{2}}^2}{\gamma_{i,K+\frac{3}{2}} - \gamma_{i,K+\frac{1}{2}}} \right]} \times \sum_J \frac{\nu_{J+\frac{1}{2}}^2 - \nu_{J-\frac{1}{2}}^2}{\nu_{J+\frac{1}{2}} - \nu_{J-\frac{1}{2}}} \int_J \int_{K+1} \frac{j_{\text{synch}}^i(\nu, \gamma_i)}{\nu} d\gamma_i d\nu. \quad (\text{B.8})$$

This choice of the flux preserves the total energy of the system, while the particle number conservation is ensured by the structure of Equation B.4. However, this choice of numerical discretization leads to numerical diffusion, see C1, in which the current scheme is compared to the classical Chang and Cooper scheme (Chang & Cooper 1970).

For the Compton scattering process, the weak formulation is trivially obtained and does not require the use of integration by part, since the kinetic equation does not take the form of a diffusion equation. For all other processes, their respective kinetic equation takes either the same form as that of synchrotron mechanism or of Compton scattering. Therefore, all energy discretization can be easily obtained following the same procedure outlined above. We note, that we use redistribution of particles in integro-differential equation type to preserve simultaneously total particle number (when required by the process) and total energy.

Before discussing the temporal discretization, we note that the equation are non-linear in the distribution function for Compton scattering, pair production, photo-pion and photo-pair processes. We decided to linearize the kinetic equations of photo-pion and photo-pair processes by assuming that the target photon-field is equal to the one at the previous time step, effectively making those process linear in the distribution functions. For all leptonic processes, we preserve the non-linearity of the kinetic equations and solve at each time step a non-linear system via the Newton-Raphson method. Since the gradients can be computed analytically, we do not need to use numerical estimates for the Jacobian. The temporal evolution of the distribution function is performed with the first order implicit Euler method.

One time step of the code takes the following form

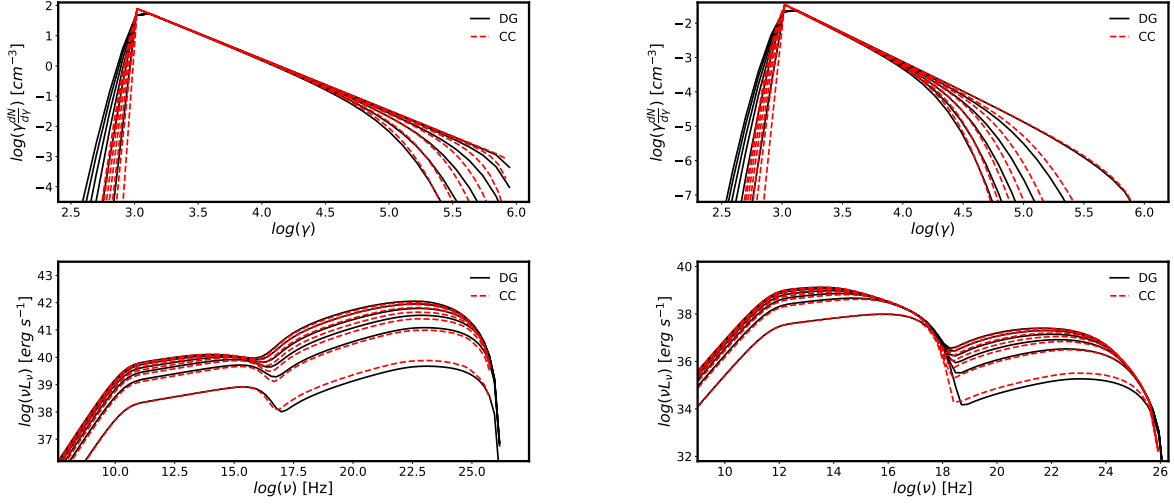


Figure C1. Comparison between the [Chang & Cooper \(1970\)](#) scheme and *SOPRANO* for Compton scattering and synchrotron radiation in two different regimes, whose parameters are given in Table C1. Left – inverse Compton dominates. Right – synchrotron cooling dominates. The plots show the time evolution of the electron (top) and photon (bottom) distribution functions up to dynamical time scale, in the comoving frame. Electron number conservation is satisfied to machine accuracy (10^{-16}) while the energy is conserved to an accuracy better than 10^{-11} .

	IC dominance	Syn dominance
$R/10^{17}$ cm	1	1
B [G]	0.005	0.1
$\gamma_{e,\min}$	10^3	10^3
$\gamma_{e,\max}$	9×10^5	9×10^5
α_e	2.7	2.7
U_e/U_B	10^5	0.1

Table C1. Parameters used for our numerical comparison between *SOPRANO* and the Chang and Cooper scheme [Chang & Cooper \(1970\)](#). The corresponding evolution of the photon and electron distribution functions is given on Figure C1.

(i) solve the linear kinetic equation to obtain the protons and neutrons spectra at time $t + dt$, assuming that the photon distribution function is given at time t for photo-pion and photo-pair processes. The pairs and photons created in those two processes and by the proton synchrotron process are saved to be used as a source term in the leptonic computation.

(ii) compute the decay and cooling (when required) of pions and muons. The pairs and photons created in the muon and pion decay, as well as their synchrotron radiation are saved to be used as source terms in the leptonic computation.

(iii) perform the non-linear implicit leptonic computation with the source terms computed in the two previous steps.

APPENDIX C: CODE TESTS AND EXAMPLES

C1 Synchrotron and inverse Compton cooling for electrons

In this section, we present two tests performed for the synchrotron and inverse Compton radiation processes. First, the results from *SOPRANO* are compared to the results obtain with our implementation of the [Chang & Cooper \(1970\)](#) scheme, which is widely spread and used in time-dependent application, see *e.g.* [Chiaberge & Ghisellini \(1999\)](#); [Gao et al. \(2017\)](#). We consider a situation in which electrons are continuously injected into the radiating zone in the form of a power-law between $\gamma_{\min} = 10^3$ and $\gamma_{\max} = 9 \times 10^5$. The properties of the radiating zone are such that for one test, inverse Compton cooling dominates over synchrotron cooling, while for the other test it is the opposite. The parameter are summarized in Table C1.

Figure C1 shows the results. It is clear that the agreement between the Chang and Cooper scheme and *SOPRANO* is very good for both the electron and the photon distribution functions. We notice that *SOPRANO* is more diffusive at low energy below the peak of the electron distribution function. This is mostly because of the scheme used to preserve the total energy of the system in *SOPRANO*, which induces extra diffusion. However, despite these differences for the electron distribution function, the photon spectra are in very good agreement.

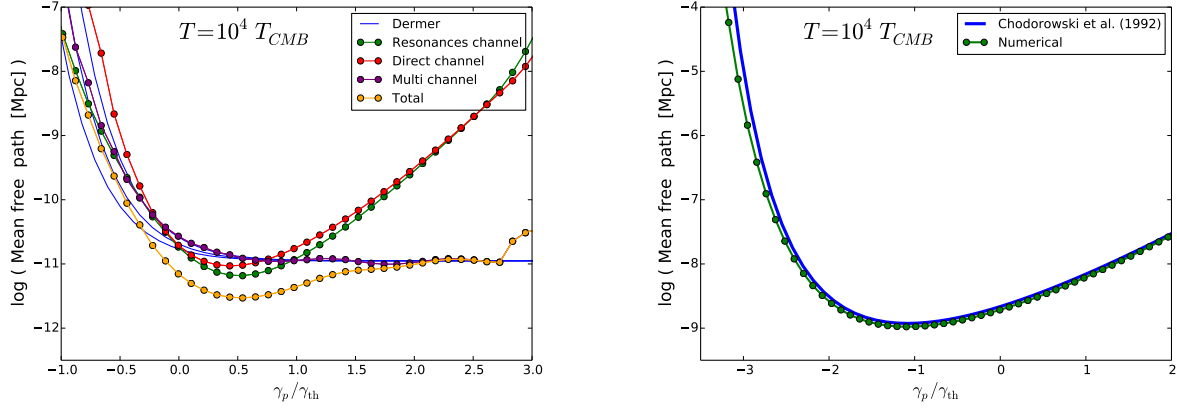


Figure C2. Right : Proton mean free path as a function of their Lorentz factor for the photon-pion process. The photon temperature is $T = 10^4 T_{\text{CMB}}$. Blue : mean free path computed by using Equation C.1 for the lower boundary center and upper boundary of an energy cell. The Lorentz factor is normalized by $\gamma_{\text{th}} = \epsilon_{\text{th}}/(2k_B \theta) \sim 3.2 \times 10^7$. Right : Proton mean free path as a function of the Lorentz factor for the photo-pair process. Green - *SOPRANO*. Blue with the approximation of Chodorowski et al. (1992). For easy comparison, the proton Lorentz factor is also normalized by γ_{th} .

C2 Proton cooling on black-body photons by photo-pair and photo-pion interaction

We start by computing the proton cooling time in photo-pion production. Atoyan & Dermer (2003) presented a simple model for the cross-section and inelasticity for the photon-pion interaction. The model is such that the product of the cross-section with the inelasticity is constant for all energies larger than the threshold energy in the center of mass frame. It gives a simple estimate of the cooling time for a proton of Lorentz factor γ_p interacting with an isotropic photon field with the spectrum of a black-body with the temperature θ . From Dermer & Menon (2009), it reads

$$t_{p\gamma}^{-1}(\gamma_p) = \frac{8\pi c \sigma_K \theta^3}{\lambda_c^3} \int_{\omega}^{\infty} dy \frac{y^2 - \omega^2}{\exp(y) - 1}, \quad (\text{C.1})$$

where λ_c is the Compton wavelength, $\sigma_K \sim 70 \mu\text{b}$ and

$$\omega = \frac{\epsilon_{\text{th}}}{2\gamma_p \theta}. \quad (\text{C.2})$$

In Figure C2, we present the mean free path in Mpc as a function of proton Lorentz factor for an hypothetical radiation field with temperature $10^4 T_{\text{CMB}}$, with the temperature of the cosmic microwave background $T_{\text{CMB}} = 2.725\text{K}$. To obtain this plot, we considered a δ -function in each of the proton energy grid bins. We see that the agreement is quite good. We remark that the contribution of the multi-production channel has a sharp increase at large Lorentz factor. This is not physical and is a grid effect. Indeed, the proton cooling is computed by summation over all created pions. Because both the pion and proton energy grid have the same maximum Lorentz factor, protons at the highest energies in our grid do not interact substantially, since they cannot create pions of the correct energy.

We now turn to the photo-pair process. The energy loss rate for this process can be written as

$$\frac{dE}{dt} = \alpha_f r_e^2 c m_e c^2 \int_2^{\infty} d\epsilon n_{\text{ph}} \left(\frac{\epsilon}{2\gamma_p} \right) \frac{\phi(\epsilon)}{\epsilon^2}. \quad (\text{C.3})$$

Chodorowski et al. (1992) gives a convenient approximation for the differential cross-section $\phi(\epsilon)$, see their appendix. It is therefore easy to compute the energy loss pathlength $r = c[(dE/dt)/E]^{-1}$. A comparison between this semi-analytical approach and our numerical discretization is given by the right part of Figure C2. We see that the agreement is excellent.

C3 Decay time

We show in this subsection how particles decay in our code with the examples of pion decay. We inject pions with a specific Lorentz factor and simulate the evolution of the system as they decay, producing neutrinos and muons. The initial pions Lorentz factor are $\gamma_\pi = 10^7, 10^8, 10^9$. In this section only, we assume that muons cannot decay. Figure C3 shows the evolution of the pion, neutrino and muon numbers as time evolve. The muon and neutrino number is obtained by summing over their respective distribution function. The same figure also shows the evolution of particle number and total energy of the system, which can be seen to be satisfied to accuracy better than 10^{-13} after 4×10^3 iterations.

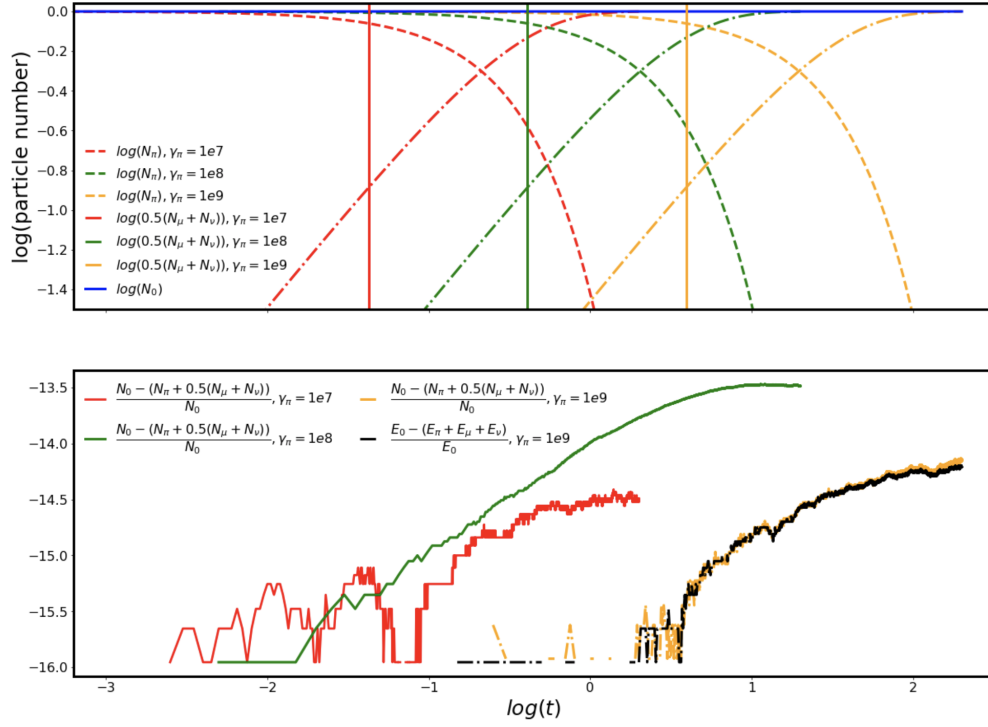


Figure C3. Top - evolution of the pion, neutrino and muon numbers as a function of time for the pion decay process. The vertical lines correspond to the decay time of the corresponding particle Lorentz factor. Obviously the decay time is properly respected. Bottom - temporal evolution of the particle number conservation and energy conservation. The total energy conservation is only shown for $\gamma_{pi} = 10^9$, but similar results are obtained for other particle energy.